Icarus **157**, 436–455 (2002)
doi:10.1006/icar.2002.6848

Dust on the Outskirts of the Jovian System

Alexander V. Krivov[1]

AG "Nichtlineare Dynamik," Institut für Physik, Universität Potsdam, Postfach 601553, 14415 Potsdam, Germany
E-mail: krivov@agnld.uni-potsdam.de

Ingo Wardinski

Geoforschungszentrum Potsdam, Telegrafenberg F456, 14473 Potsdam, Germany

Frank Spahn

AG "Nichtlineare Dynamik," Institut für Physik, Universität Potsdam, Postfach 601553, 14415 Potsdam, Germany

and

Harald Krüger and Eberhard Grün

Max-Planck-Institut für Kernphysik, Postfach 103980, 69029 Heidelberg, Germany

Received August 15, 2001; revised February 27, 2002

The outer region of the jovian system between ∼50 and 300 jovian radii from the planet is found to be the host of a previously unknown dust population. We used the data from the dust detector aboard the Galileo spacecraft collected from December 1995 to April 2001 during Galileo's numerous traverses of the outer jovian system. Analyzing the ion amplitudes, calibrated masses and speeds of grains, and impact directions, we found about 100 individual events fully compatible with impacts of grains moving around Jupiter in bound orbits. These grains have moderate eccentricities and a wide range of inclinations—from prograde to retrograde ones. The radial number density profile of the micrometer-sized dust is nearly flat between about 50 and 300 jovian radii. The absolute number density level (∼10 km^{-3} with a factor of 2 or 3 uncertainty) surpasses by an order of magnitude that of the interplanetary background. We identify the sources of the bound grains with outer irregular satellites of Jupiter. Six outer tiny moons are orbiting the planet in prograde and fourteen in retrograde orbits. These moons are subject to continuous bombardment by interplanetary micrometeoroids. Hypervelocity impacts create ejecta, nearly all of which get injected into circumjovian space. Our analytic and numerical study of the ejecta dynamics shows that micrometer-sized particles from both satellite families, although strongly perturbed by solar tidal gravity and radiation pressure, would stay in bound orbits for hundreds of thousands of years as do a fraction of smaller grains, several tenths of a micrometer in radius, ejected from the prograde moons. Different-sized ejecta remain confined to spheroidal clouds embracing the orbits of the parent moons, with appreciable asymmetries created by the radiation pressure and solar gravity perturbations. Spatial location of the impacts, mass distribution, speeds, orbital inclinations, and number density of dust derived from the data are all consistent with the dynamical model.

Key Words: **interplanetary dust; satellites of Jupiter; planetary rings.**

1. INTRODUCTION

In this paper, we focus our investigations on the outer part of the jovian system outside the orbits of the Galilean satellites. That region harbors two groups of small moons, a prograde family of five satellites between 155 and 177 R_J (jovian radii) and a retrograde group of 14 moons between 285 and 339 R_J. Of these, ten moons (one prograde and nine retrograde) were discovered in 2000 (Sheppard *et al.* 2000). Subsequently, another small satellite (temporary designation S/2000J1) was discovered closer to Jupiter at 104 R_J from the planet (Sheppard *et al.* 2001). All 20 moons, often called irregular satellites, are thought to have been captured from heliocentric orbits (e.g., Cruikshank *et al.* 1982).

Atmosphereless planetary satellites in the Solar System are well known to be sources of tenuous circumplanetary dust structures. Dust is kicked off the satellite surfaces by impacts of micrometeoroids, mostly of interplanetary origin. Examples are the saturnian E-ring (Horányi *et al.* 1992) and G-ring (Throop and Esposito 1998), the broad dusty bands of Uranus (Esposito and Colwell 1989), as well as dust in the ring system of Neptune (Colwell and Esposito 1990). In the jovian system, two gossamer

[1] On leave from Astronomical Institute, St. Petersburg University, Stary Peterhof, 198504 St. Petersburg, Russia.

0019-1035/02 $35.00

rings are maintained through the impact ejection mechanism by four innermost satellites (Burns *et al*. 1999, Ockert-Bell *et al*. 1999). Krivov *et al*. (2002) argue for the existence of an extremely tenuous ring encompassing the orbits of the Galilean moons. Here we propose that an even more tenuous, yet detectable by in-situ measurements, dust cloud is associated with the outer irregular satellites.

First in-situ measurements of dust at Jupiter were made by Pioneer-10 and Pioneer-11 spacecraft in the 1970s and more recently by Ulysses during its flyby of Jupiter in 1992. Although few dust detections have been made, these hyperbolic flybys were too short to provide any definite conclusions about the jovian dust environment beyond the orbits of the Galilean satellites (Humes 1976, Kessler 1981, Zook and Su 1982). The main bulk of the data used here to search for planetary dust in the outer part of the jovian system comes from the dust detector onboard the Galileo spacecraft (Grün *et al*. 1992). Galileo has been orbiting Jupiter since December 1995 and has completed more than 30 revolutions around the planet by now. The more than five-year long dust data set, covering the period from December 1995 through April 2001, is available (see Krüger *et al*. 2001, and details therein, http://www.mpi-hd.mpg.de/dustgroup/galileo), offering an excellent opportunity to inspect the low-density dust environment on the outskirts of the jovian system.

The dust detector data of the Galileo spacecraft are analyzed in Section 2. In Section 3, we model the production, orbital dynamics, and distribution of the ejecta from the prograde and retrograde moons. A detailed comparison of the data analysis and the theoretical results is made in Section 4. Section 5 lists our conclusions.

2. DATA ANALYSIS

2.1. *Dust Impact Data*

The Galileo dust detector system (DDS) is an impact ionization dust detector (Grün *et al*. 1992). Three independent charge signals (ion amplitude *IA*, electron amplitude *EA*, and channeltron amplitude *CA*) of the impact-created plasma cloud are used to classify each impact event (Grün *et al*. 1995b, Krüger *et al*. 1999a). Impact events are divided into four quality classes (*CLN*) and six ion amplitude ranges (*AR*). While *CLN* = 3 events are real dust impacts, events of the lower quality classes are contaminated by noise (Grün *et al*. 1995a, 1997, 1998, Krüger *et al*. 1999b). On the average, the lower the class, the larger the fraction of noise events. Each of the *AR*s corresponds to 1 order of magnitude of the impact charge and is further subdivided into eight digital *IA* values. *AR* = 1 includes *IA* from 0 to 7, *AR* = 2 from 8 to 15, and so on. The smaller the *AR* (or *IA*), the lower the impact energy.

The charge Q_I released upon impact has been used to calibrate the DDS for impact velocities of the grains between 2 and 70 km s^{-1} and grain masses between 10^{-6} and 10^{-16} g. Earth-based experiments yielded an empirical relation between Q_I, mass M of a grain and its speed v (Grün *et al*. 1992, 1995a):

$$Q_I \propto M\, v^{3.5}. \qquad (1)$$

Another measurable quantity is the charge rise time. It depends on the impact speed v alone, which allows decoupling M and v in Eq. (1). The derived values of the speed and mass of a particle are uncertain by a factor of about 2 and 10, respectively (Grün *et al*. 1992, their Fig. 8). Like *CLN*, *AR*, and *IA*, calibrated masses and speeds of the grains are part of the DDS data set.

2.2. *Impact Geometry*

Most of the time, the Galileo antenna points toward the Earth, and the dust detector spins together with the spacecraft around an axis which points in an anti-Earth direction (Fig. 1). The axis of the detector is at 60° to this spin axis. The position of the detector with respect to the spin axis, i.e., the so-called rotation angle *ROT*, is recorded for each impact. The direction of increasing *ROT* is opposite to the spin direction of the spacecraft (Grün *et al*. 1995a). *ROT* = 0 is the direction closest to the ecliptic north. The value of *ROT*, together with the orientation of the spacecraft spin axis, provides the direction information on the events. Because it is not possible to determine from where in the 140° cone of the detector's field of view a particle comes, there is a systematic uncertainty of ±70° in retrieving the impact direction. For instance, particles approaching from close to the ecliptic plane will be detected either from *ROT* = 270° ± 70° or *ROT* = 90° ± 70°.

The total sensitive area A_0 of the detector is 1000 cm^2. However, the effective sensitive area A_S available for the detection of particles is usually smaller due to an angle ϕ between the

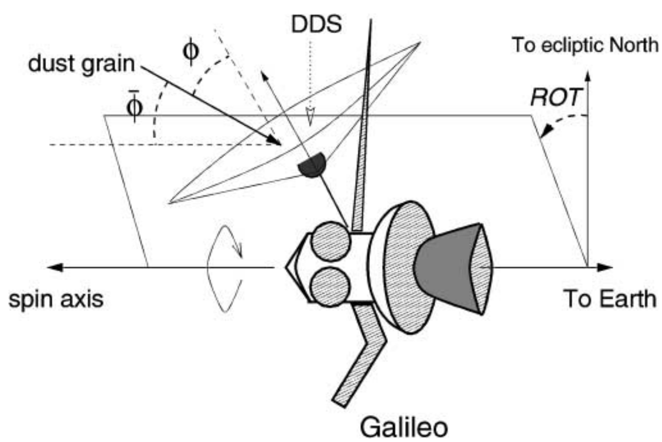

FIG. 1. Detection geometry. The instantaneous impact angle ϕ is the angle between the relative velocity vector of a dust grain and the symmetry axis of the sensor. The "averaged" impact angle $\bar{\phi}$ is the angle between the vector of impact velocity of a dust particle and Galileo's negative spin axis which points away from the Earth. The instantaneous pointing of the DDS is determined by the rotational angle *ROT*.

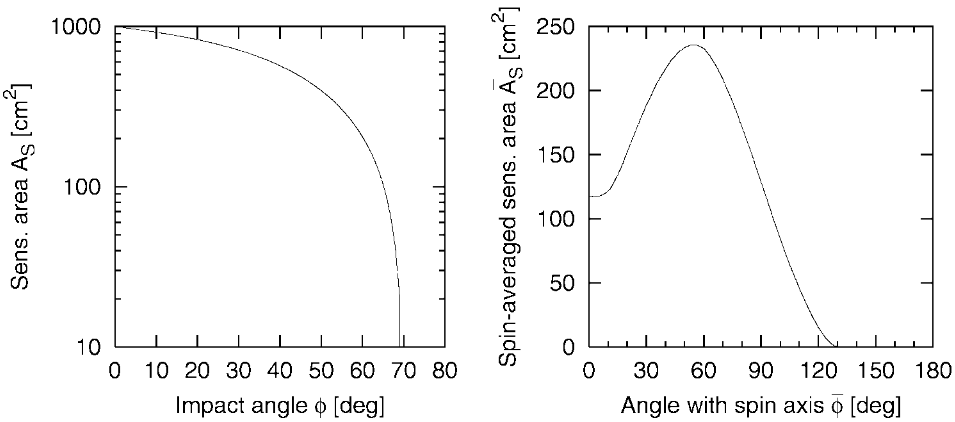

FIG. 2. Left: Sensitive area A_S of the Galileo dust detector as a function of the impact angle ϕ. Right: Effective sensitive area $\bar{A}_S$ of the Galileo dust detector, averaged over one rotation period of the spacecraft, as a function of the angle with the spin axis $\bar{\phi}$.

relative velocity vector and the direction of the sensor. The function $A_S(\phi)$ from Krüger *et al.* (1999b) (their Fig. 10) is plotted in Fig. 2 (left). This curve was determined for events with $CLN \geq 2$, but can also be applied to $CLN = 0$ and 1.

To analyze the sensitivity of DDS to dust impacts over longer time spans, it is convenient to introduce the effective sensitive area $\bar{A}_S$, averaged over one spin revolution of Galileo (about 20 seconds). The spin-averaged effective area depends on the "averaged impact angle" $\bar{\phi}$, the angle between the impact velocity vector of a dust grain, and the negative spin axis of Galileo (Fig. 1). The function $\bar{A}_S(\bar{\phi})$ from Krüger *et al.* (1999b, their Fig. 11) is plotted in Fig. 2 (right). The maximum value of $\bar{A}_S$ is about $235\,\text{cm}^2$ for $\bar{\phi} \approx 55^\circ$ (Krüger *et al.* 1999b; see also Grün *et al.* 1992). For smaller values of $\bar{\phi}$, $\bar{A}_S$ reduces to about $120\,\text{cm}^2$ at $\bar{\phi} = 0$. For larger $\bar{\phi}$, $\bar{A}_S$ decreases continuously down to zero for $\bar{\phi} \approx 130^\circ$.

2.3. *The Orbital Tour of Galileo*

Galileo entered the jovian system in December 1995 and has made more than 30 orbital revolutions about Jupiter. Each orbit is labeled with the first letter of the Galilean satellite (or Jupiter), which was the encounter target during that orbit, followed by the orbit number. Henceforth, by "Galileo orbit" we mean the period between two consecutive perijoves: e.g., the *G28* orbit covers the time between the perijove of the *G28* encounter (day 00–142) and the perijove of the *G29* encounter (day 00–364). In what follows, the initial leg of the Galileo trajectory before the first perijove will be referred to as *JOI* leg (*JOI* stands for Jupiter Orbit Insertion).

From earlier to later orbits, the line of apsides was turning clockwise in the synodic jovicentric coordinate system, so that the measurements have covered up to now the whole anti-solar side of the outer jovian system (Fig. 3). The initial leg (*JOI*) brought measurements at all distances from the planet, and the first bound orbit (*J0*) had an apojove at $\approx 270 R_J$. The "middle" orbits from (*G1*) to (*I27*) all had apojoves at $\lesssim 150 R_J$. The latest orbits *G28* and *G29* brought Galileo outside $200 R_J$ again.

2.4. *Sensitivity of the DDS to Dust in Different Types of Orbits*

We will search for possible ejecta from the outer moons, moving in bound orbits around Jupiter. Modeling the dynamics of these grains (see Section 3) shows that they are expected to have low or moderate eccentricities e, but orbital inclinations i in a wide range from nearly 0° to 180°. For the following sensitivity analysis, we therefore introduce four idealized types of orbits: prograde ones with $i = 0^\circ$; retrograde with $i = 180^\circ$; polar with $i = 90^\circ$ that reach DDS at the ascending node (the orbital velocity vector points to the ecliptic north); and polar that hit the detector at the descending node (the velocity vector is directed to the south). We will call them, for brevity, p-, r-, a-, and d-orbits, respectively. In so doing, we generalize the analysis of Thiessenhusen *et al.* (2000) who considered p- and r-orbits only in their study of dust in the region of the Galilean satellites. All these orbits are assumed to be circular ($e = 0$). To get a rough idea of a possible contribution made by particles in eccentric orbits, we introduce one more class of idealized orbits—"levitating" grains, motionless with respect to Jupiter and hence approaching the detector from the ram direction. Such grains would model particles in very eccentric orbits with arbitrary inclinations that spend most of their time near the apocenter where their speed is very low. We will refer to this case as "e-orbits."

The rotation of the line of apsides of the Galileo trajectory (Fig. 3), together with the fact that the Galileo spin axis was always directed approximately in the anti-solar direction, has the consequence that the sensitivity of DDS to grain orbits with various orientations steadily evolved with time. For each orbital loop of Galileo, we calculated the spin-averaged sensitivity area of DDS, $\bar{A}_S$, with respect to the five types of grain orbits introduced above. Typical results for several revolutions of Galileo are shown in Fig. 4. On the incoming *JOI* trajectory, Galileo's DDS could detect all types of particles. The sensitivity to prograde grains was higher than the sensitivity to inclined and eccentric ones, the latter, in turn, being higher than the sensitivity to retrograde particles. The first half of the *J0* orbit brought no data, because the DDS was switched off (Krüger *et al.* 2001).

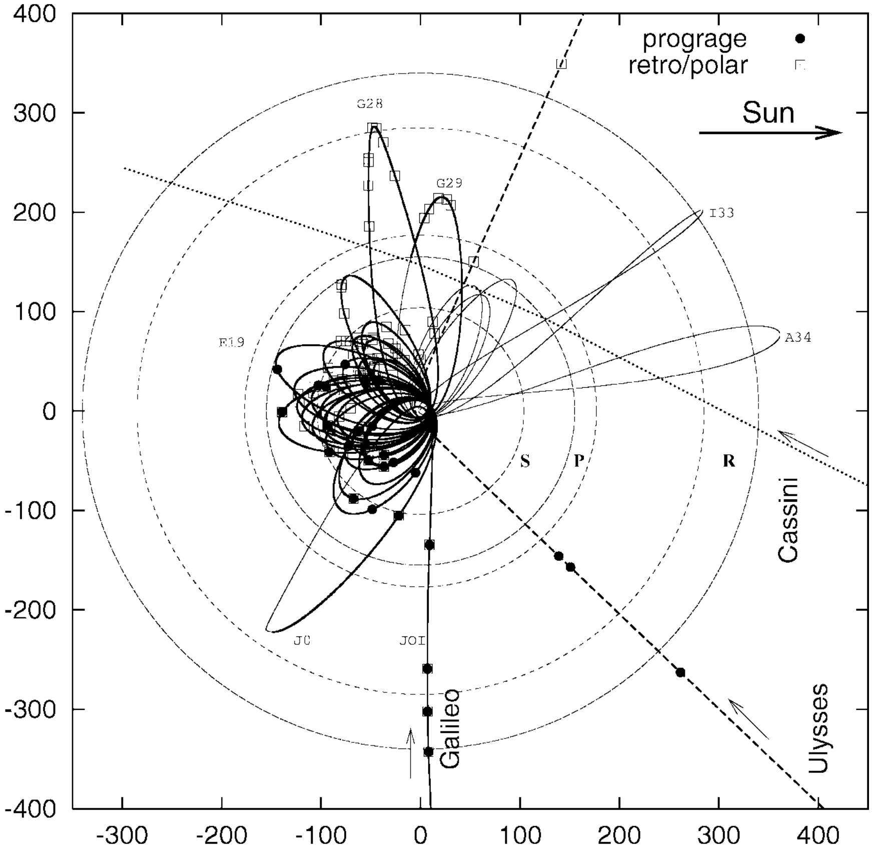

FIG. 3. Galileo and Ulysses trajectories in the jovian system and the impact events selected. Also shown is the trajectory of Cassini during its Jupiter flyby in December 2000. The thin-line part of the Galileo trajectory before the apojove of the *J0* orbit and after the apojove of *G29* marks the periods when DDS was not operating or where the data are not yet available. Symbols show the impact events with $CLN = 0, 1, 2, 3$, $IA > 7$, and $v < 10\,\mathrm{km\ s^{-1}}$. Bold dots are events compatible with impacts of prograde particles, open squares are impacts of grains possibly in retrograde or polar orbits; overlap indicates events that are compatible with all these orbits. Dashed circles centered on Jupiter mark the locations of S/2000J1 ("S"), 5 prograde ("P") and 14 retrograde ("R") irregulars.

After the apojove of *J0* the DDS had a high sensitivity to prograde grains and a moderate one to grains in highly inclined orbits. Retrograde and eccentric particles could not be detected. Starting from *J0*, there was a gradual increase of DDS average sensitivity to retrograde particles and a decrease to prograde ones. At *C9*, for instance, the DDS sensitivity to both types of grains was comparable. During the later orbits—*G28* and *G29*—Galileo DDS became highly sensitive to retrograde particles and insensitive to prograde ones. The sensitivity to the grains in polar and eccentric orbits was nearly as high as to the retrograde ones. The orbit *I33* that starts in January 2002 will drive the spacecraft to about $350R_J$ in June 2002. After the apojove, a possibility to detect prograde grains appears again for the first time after the early stage of the mission. During the final orbit *A34* before Galileo crashes into Jupiter, DDS will be nearly as sensitive to prograde grains as to retrograde ones.

2.5. *Selection of Impact Events*

We used the full Galileo dust data set (Standard Dust Data File, SDDF), which contains all events detected with the Galileo DDS (i.e., dust plus noise). The SDDF file covers the period from 1995, day 285 (Galileo, approaching Jupiter in *JOI* orbit, reached the distance $500R_J$) to 2001, day 117 (orbit *G29*). The whole data set contains 33,973 records. Many of these were noise events, as discussed below. The overwhelming majority of the remaining events took place closer to Jupiter in the region of the Galilean satellites. The data set includes impacts of tiny high-speed stream particles (Grün *et al.* 1998), electromagnetically captured interplanetary grains (Colwell *et al.* 1998), dust grains of the clouds around the Galilean satellites (Krüger *et al.* 1999c, 2000), grains that build up a tenuous dust ring between the orbits of Europa and Callisto (Krivov *et al.* 2002), and possibly dust left from the fragmentation of the Shoemaker-Levy 9 (SL9) comet (Horányi 1994). We shall sift out all these, as well as interplanetary and interstellar dust impacts, and seek the dust impacts in the outermost part of the jovian system that may be compatible with impacts of particles in bound orbits about Jupiter produced by sources, which we later identify with outer irregular moons. In constructing the event selection criteria described below, we use a cautious approach. In unclear cases, we prefer to filter out some of the events that may still be

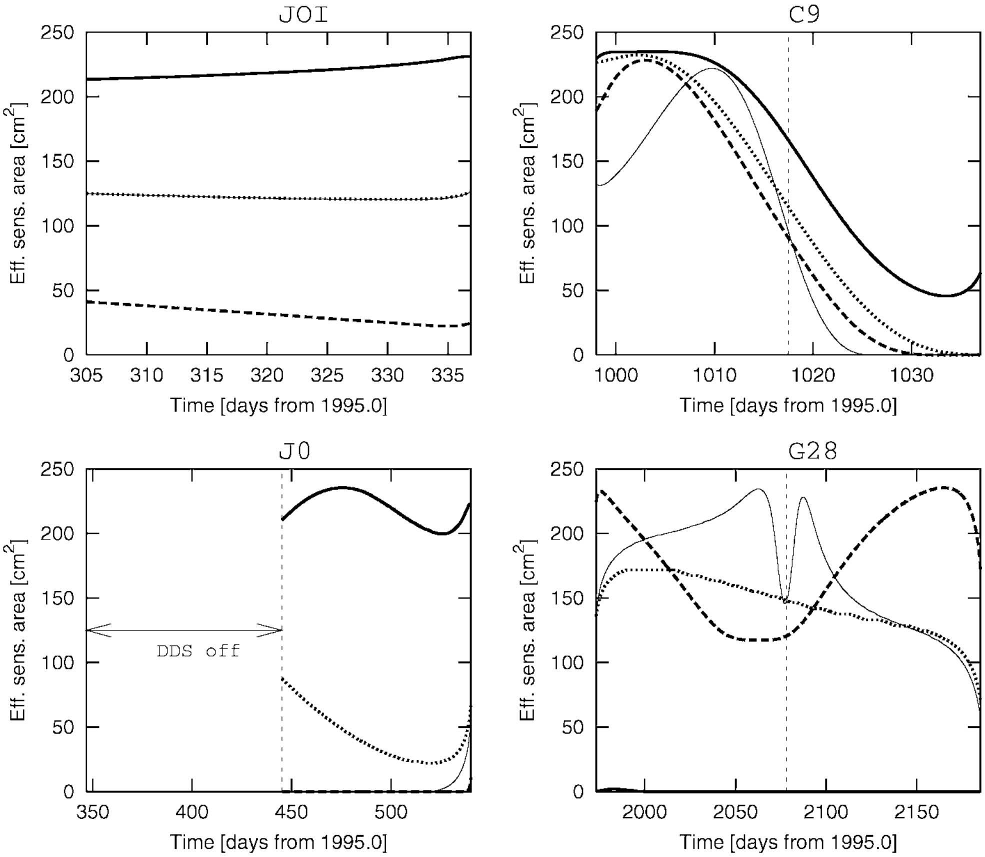

FIG. 4. Spin-averaged sensitive area of DDS with respect to different types of dust grains in circular orbits: prograde (thick solid line), retrograde (thick dashed line), polar at ascending or descending node (thick dotted line), as well as to "motionless" grains that approach the detector from the ram direction (thin solid line). As the spin axis of Galileo lies nearly in the equatorial plane, the sensitive areas for grains in ascending and descending orbits differ not more than by 10 cm^2; therefore, we show only one curve for both types of the polar orbits. Different panels depict the results of the Galileo orbits *JOI*, *J0*, *C9*, and *G28*. Each plot starts five days after a perijove and ends five days before the next perijove. A vertical straight line marks an apojove.

relevant than to retain events that may not be pertinent to this study.

We will confine our analysis to the planetocentric distance range from 50 to $500R_J$. Although these boundaries are conventional, the lower limit is chosen well outside the orbit of Callisto to avoid contribution from the ring maintained by the Galilean satellites, whereas the upper limit is taken well outside the orbits of the most distant outer satellites (but still inside Jupiter's Hill sphere with respect to the Sun, with the radius of $\approx 740R_J$).

The first problem is a possible contamination of the SDDF file with noise. The noise environment in the inner jovian system is very different from that in interplanetary space: classes 0, 1, and 2 are strongly contaminated by noise within about $20R_J$ from Jupiter. Class 3 does not show indications for noise contamination. The noise could be removed from the class 2 data in this region (Krüger *et al.* 1999b), but the lower classes 0 and 1 are noise events to almost 100%. This is the reason why other studies of the Jupiter dust environment (e.g., Krüger *et al.* 2000, Thiessenhusen *et al.* 2000, Krivov *et al.* 2002, Krüger *et al.* 2001) used the events with $CLN = 3$ and $CLN = 2$ only. On the contrary, beyond $20R_J$, the noise contamination in classes 0, 1, and 2 is very low, especially in the higher ion amplitude ranges $AR \geq 2$. By applying the denoising algorithm developed for the inner jovian system to the region beyond $20R_J$, true dust impacts are erroneously classified as noise and removed from the data set. We checked the denoised Galileo dust data set (Dust Parameter File, DPF) which contains class 3 and denoised class 2 events only. A comparison of class 2 and 3 events detected beyond $50R_J$ ($AR \geq 2$) shows that the ratio of events in both classes in the denoised data set (DPF) is systematically low. On the contrary, this ratio is similar to the value found in the low-noise interplanetary environment, if we take the full data set of all events (SDDF). This can be an indication that the lower classes ($AR \geq 2$) are basically noise-free beyond $50R_J$. We also checked whether the events in the lower quality classes occurred from preferred impact directions because—unlike dust impacts—noise events should not show preferred directions. This, however, was not conclusive because in some periods the class 2 events were concentrated toward specific impact directions but in other periods such concentrations were absent. Anyway, it is very difficult to draw any firm conclusions because of the low number of events. Events in classes 0 and 1 behave similarly, but here a check is even more difficult because the number of events is even lower. In the following analysis we used the SDDF data set and all quality classes, from $CLN = 0$ to $CLN = 3$. Nevertheless, we checked our results against the DPF file to make sure that our conclusions are not affected by the assertion that most of the records in the SDDF file outside $50R_J$ are real dust impacts.

The next task is getting rid of stream particles—ironically, because they have long been attracting most of the interest of those who study dust around Jupiter! As most of the stream particles generate impact events in $AR = 1$ (Grün *et al.* 1998, Krüger *et al.* 1999b, Thiessenhusen *et al.* 2000, Krüger *et al.* 2001), we consider events with $AR \geq 2$ ($IA > 7$) only.

To search for bound planetocentric orbits, we also make use of a speed criterion. The Keplerian circular speed ranges from $2\,\mathrm{km\,s^{-1}}$ at $350R_J$ to $6\,\mathrm{km\,s^{-1}}$ at $50R_J$. The mean Galileo speed at 100–$300R_J$ was 1–$2\,\mathrm{km\,s^{-1}}$. We thus selected the particles with calibrated impact speeds $\leq 10\,\mathrm{km\,s^{-1}}$. In accordance with Eq. (1), this automatically selects grains with calibrated masses $\geq 10^{-13}$ g (grains with radii $\gtrsim 0.2\,\mu$m). We note that in the outermost region, at $r \sim 300R_J$, the actual range of masses in the selected subset of events may be even narrower, being limited by the amplitude range condition. In that region, where impact velocities $\sim 2\,\mathrm{km\,s^{-1}}$ are expected, employing the $AR \geq 2$ criterion will result in loss of many particles with masses $M \lesssim 10^{-11}$ g—these produce impacts in the same $AR = 1$ as the stream particles. Therefore, the number densities of the $10^{-13}\,\mathrm{g} \lesssim M \lesssim 10^{-11}$ g grains we will derive will provide a lower bound on the actual values. For $M \gtrsim 10^{-11}$ g, the results should be correct.

The resulting impact record contains more than 2000 events, of which only 99 took place outside $50R_J$, including 15 outside $200R_J$. The latter subset is given in Table I. Interestingly, most of these events have high quality ($CLN = 2$ and 3; class 0 is completely absent). The number of grains with masses $> 10^{-11}$ g outside $50R_J$ is 69, including 9 outside $200R_J$.

Could the data set be contaminated by impacts of background, interplanetary and interstellar, particles? The speed criterion $v \leq 10\,\mathrm{km\,s^{-1}}$ suggests that most of the latter, with their typical speed of $\approx 26\,\mathrm{km\,s^{-1}}$ (Grün *et al.* 1994), are automatically removed. Still, as the calibrated velocities may be in error by a factor of 2 (Grün *et al.* 1992), a small fraction of the selected events may be caused by impacts of interstellar particles. And conversely, a minor fraction of faster jovicentric grains may have calibrated speeds larger than $10\,\mathrm{km\,s^{-1}}$ and will be lost for the analysis. Nevertheless, this speed criterion is believed to be a reasonable compromise.

Filtering out the interplanetary particles represents a much more serious problem. To estimate the influence of the interplanetary (and interstellar) background, we use a natural idea: to check the events registered by the same detector, Galileo DDS, close enough to Jupiter, but safely outside the region where the jovian dust is expected. We chose the part of the initial *JOI* trajectory from the beginning of 1995 untill 1995, day 285—the jovicentric distance range from 2400 to $500R_J$. We applied exactly the same criteria as described above: *CLN* from 0 to 3, $IA > 7$, $v \leq 10\,\mathrm{km\,s^{-1}}$. During this period, 15 events were found, and these were interpreted as impacts of interplanetary grains with a possible minor fraction of interstellar ones. Figure 5 (top) shows the mass distribution of these background grains which, for masses $\gtrsim 3 \times 10^{-13}$ g, is a decreasing, power-law like, function of mass—quite as expected. We conclude that, on the average, about one impact per 20 days can be attributed to the background particles. For particles with masses $> 10^{-11}$ g, the rate reduces to about one hit per 70 days (four events detected in 285 days). Note that the gravitational focusing of the external

TABLE I
Selected Impact Events with $IA > 7$ and $v < 10\ \mathrm{km\,s^{-1}}$ outside $200R_J$

								Eff. sens. area [cm^2]				
YY-DDD	*CLN*	*AR*	*IA*	Mass [g]	Speed [km s^{-1}]	r [R_J]	*ROT* [deg]	p	a	r	d	e
95-304	2	2	9	5.3e-13	9.7	343.97	15	212	0	0	668	0
95-310	1	2	9	2.3e-13	9.7	303.21	0	205	0	0	711	0
95-315	2	2	11	3.1e-13	9.7	260.25	329	189	0	0	535	183
00-195	3	3	20	9.3e-11	4.5	238.01	353	0	0	186	701	0
00-219	2	2	8	1.8e-11	2.3	272.97	177	0	709	207	0	0
00-242	2	2	10	1.5e-11	3.8	288.14	30	0	0	287	546	0
00-242	2	2	8	7.9e-12	3.8	288.14	149	0	535	289	0	0
00-260	3	2	8	4.8e-11	2.7	289.08	345	0	0	146	668	0
00-297	1	2	9	4.9e-10	2.0	259.08	138	0	399	348	0	308
00-299	2	2	8	1.5e-12	4.5	255.92	35	0	0	327	489	261
00-312	1	2	9	5.5e-11	2.0	232.65	339	0	0	96	628	0
01-054	2	2	15	3.3e-10	2.5	209.30	13	0	0	161	678	0
01-062	2	2	10	2.1e-11	4.5	214.51	335	0	0	260	594	434
01-077	3	3	21	8.2e-11	6.4	215.07	218	0	452	262	0	0
01-092	2	2	8	1.7e-13	9.7	203.65	110	0	0	159	0	843

Note. See Section 2 for notation.

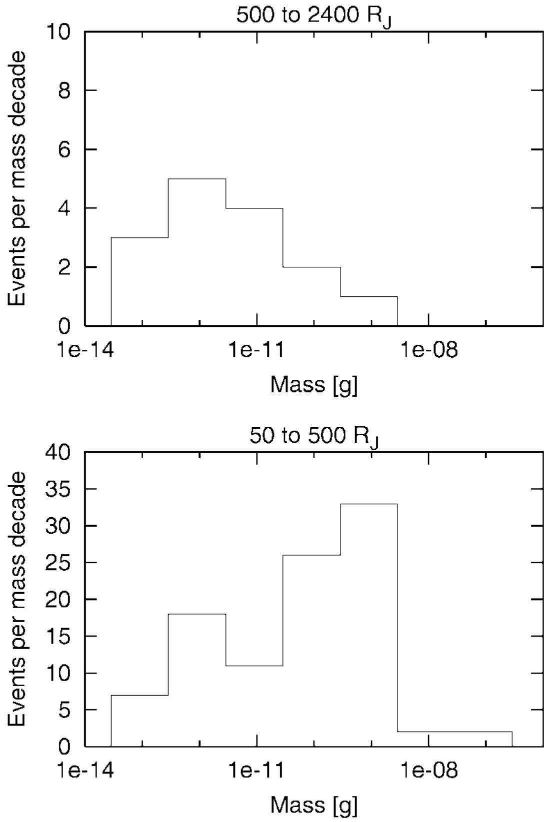

FIG. 5. Number of impacts per mass decade for selected events "far" from Jupiter (top) and in the outer part of the jovian system (bottom). The leftmost bins are centered on $M = 10^{-13}$ g. For comparison, the detection threshold for impact events with $IA > 7$ is 6×10^{-13} g for $v = 10\,\mathrm{km\,s^{-1}}$ and 7.5×10^{-11} g for $v = 2.3\,\mathrm{km\,s^{-1}}$, respectively (see Section 2.5).

particles by Jupiter does not introduce any tangible correction to these estimates: assuming the speed of interplanetary grains prior to focusing of $\approx 20\,\mathrm{km\,s^{-1}}$ (Krüger *et al.* 2000), their flux increases at most by 20% at $50R_J$.

These impact rates should be corrected for incomplete data transmission (Krüger *et al.* 1999a). Because Galileo has a low data transmission capability, full data sets for some of the impact events have not been transmitted to the Earth. Nevertheless, all events are counted by the dust instrument, so the completeness of the data set can be determined. We analyzed the accumulator records during the *JOI* trajectory between 2400 and $500R_J$ to find that 75 events with $IA > 7$ and all quality classes were counted by the accumulators, of which 52 were transmitted with their complete data sets. This gives a completeness factor of 70%. Therefore, the corrected impact rate of background particles would be 1 hit of a $>10^{-11}$ g grain in about 50 days.

Of course, these estimates apply only to the events that satisfy our selection criteria and thus these numbers do not represent the full impact rate of interplanetary particles onto DDS. Unfortunately, there is no reliable way to identify and eliminate the interplanetary particles from the selected subset of events. Therefore, the above estimates will be used below to estimate the significance of the background contamination statistically.

2.6. *Analysis of Impact Events*

Next, we wish to retrieve information about the orbits of the selected grains—most notably, to estimate which type of the orbits (circular prograde, polar, retrograde, or eccentric) the impacted grains had. To do this, we employed, for each of the events individually, the following procedure. Using the rotation angle at the moment of a *real* impact, *ROT*, we calculated the instantaneous direction of the DDS symmetry axis, **l**. Then we considered five types of orbits of *hypothesized* grains—p-, r-, a-, d-, and e-ones. For each type, given the position and velocity of Galileo at the moment of impact, we calculated the impact velocity vector that the hypothesized grain would have, **v**. The angle between **l** and −**v** is then the simulated impact angle ϕ. Given this angle, we determined the corresponding sensitive area of DDS, A_S (Fig. 2, left). This gives us, for each impact event, five values: the sensitive area of the dust detector with respect to prograde, retrograde, two types of polar, and eccentric (ram) grains. These values, listed in the last columns in Table I, show which type of orbit the impacted grain could have. In some cases, we can draw a definite conclusion (of course, within the adopted orbit classification scheme): for instance, event 95-310 (Table I) could have only been caused by a grain in southbound polar circular orbit. In most cases, however, only a probabilistic conclusion is possible. For example, event 01-077 was most likely caused by a grain moving in a nearly-polar orbit from south to north, but (less probably) could have resulted from a grain in retrograde orbit.

In Fig. 6 we plot the calibrated masses of impacted grains against distance from Jupiter. We show the results for all impacts registered, as well as for p-, r-, a-, d-, and e-particles separately. Henceforth, by "p-particles," for instance, we mean all the grains that *could* have been moving in prograde orbits and not those that *did* move in such orbits. In other words, we classify into "p-case" those impact events for which the sensitive area of DDS with respect to dust in prograde orbits was nonzero, whether or not A_S was nonzero with respect to other types of orbits as well. For example, event 01-062 (Table I) appears on r-, d-, and e-plots.

Two populations of dust are seen in Fig. 6. The first population is dust between $\sim 50R_J$ and $\sim 150R_J$ (the orbits of the prograde irregulars), which does not show any preferential type of orbits. Later on, we shall see that many of these grains are compatible with being ejecta from the prograde irregular moons. The second population is the one outside about $150R_J$. The data are incompatible with prograde orbits and only few events are compatible with low-speed "e-grains." These particles may, therefore, have come from the retrograde irregular moons. We note that all these grains were detected inside $350R_J$. Galileo was outside this distance only during its initial approach of Jupiter (*JOI* orbit), during which it was nearly insensitive to retrograde orbits, but could detect dust in prograde or polar orbits. No impacts satisfying our selection criteria were detected for this time period.

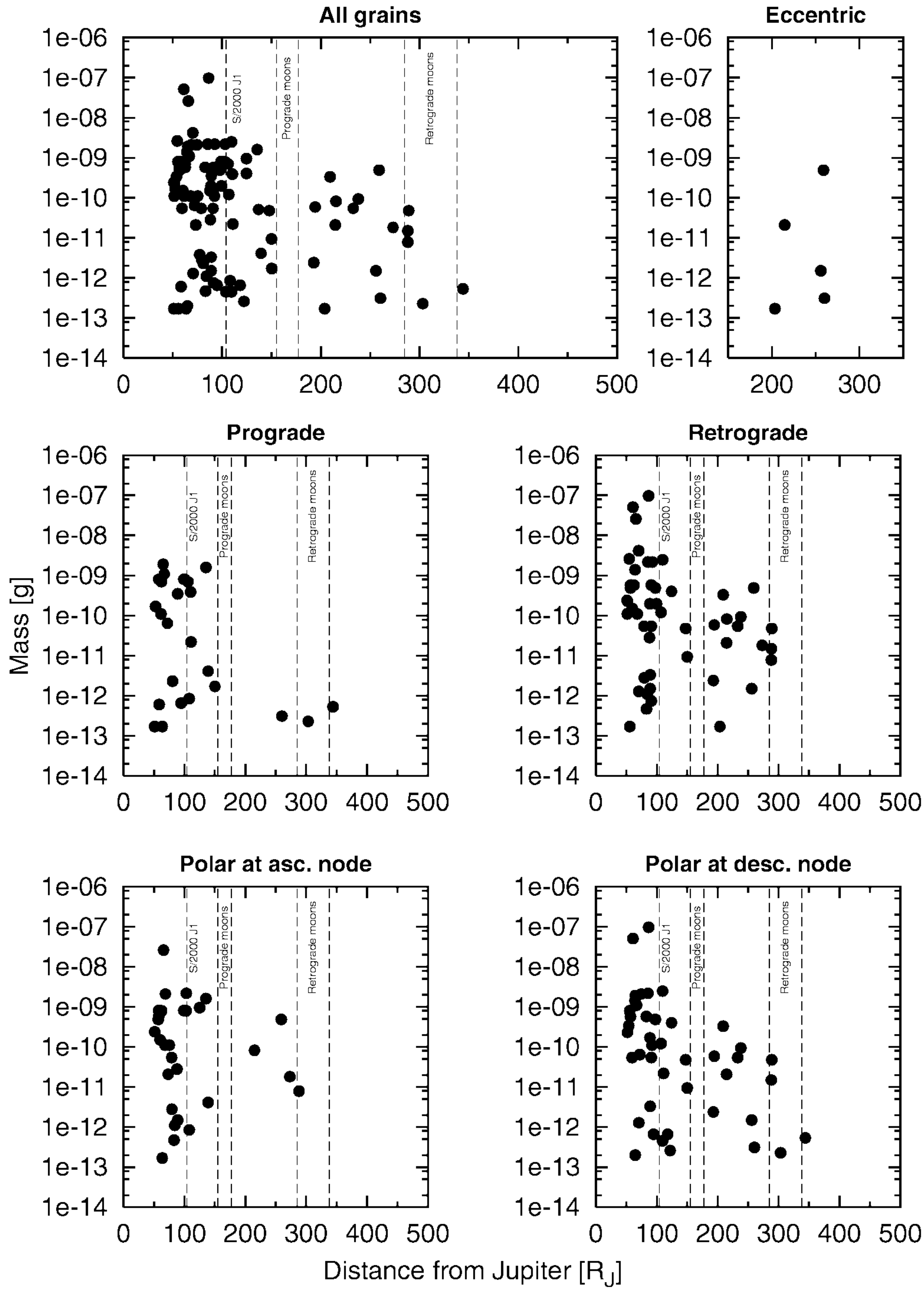

FIG. 6. Dust impacts with $IA > 7$ and $v < 10\,\mathrm{km\,s^{-1}}$ outside $50R_J$: calibrated masses versus distance from Jupiter. Left top panel: all impact events, four lower panels: impacts of dust grains compatible with prograde, retrograde, and two types of polar circular orbits. Right top panel shows impacts of particles that could be attributed to impacts of grains nearly motionless about Jupiter (i.e., particles on very eccentric orbits near apocenters). Thin vertical lines mark the orbit of S/2000J1, the zone of 5 prograde moons, and the region of 14 retrograde moons.

We note that Fig. 6 does not allow one to make any conclusions about the number density of dust in different populations. Namely, the "density" of points that decreases with the increasing distance from Jupiter does not necessarily imply that the number density does. One reason is that Galileo spent quite different time periods at different distances from the planet. Besides, DDS had different sensitivity at different distances and the mean impact speed of the grains is a function of distance as well. The number density of dust grains is computed in the next section, taking full account of all these effects.

Another type of information provided by Fig. 6 is a distribution of particle masses. An interesting effect is seen: throughout the outer region, the mass range around (or slightly below) 10^{-11} g turns out to be relatively devoid of dust, which is seen even clearer in the bottom panel of Fig. 5. For a bulk density of about 2 g cm^{-3}, the position of the gap corresponds to grains with radii just below 1 μm. We will suggest a possible explanation in Section 3. In particular, as we shall see below, a significant fraction of the particles with masses below the "mass gap" (the left peak in the bottom panel of Figure 5 and grains in the bottom part of Fig. 6 panels) are very likely exogenic, interplanetary particles.

2.7. *Number Density*

We now calculate the number density of dust at different distances from Jupiter. To this end, we divide the whole distance range considered (up to $500R_J$) into equal bins with a width of $50R_J$. The following procedure was then applied to each bin:

1. From all impact events, previously selected by the *IA* and speed criteria, we extract those that fall into the bin. This gives us the number of events in the bin, $N_{\rm bin}$.
2. From the spacecraft trajectory file, we compute the time that Galileo spent in the bin, $T_{\rm bin}$. Only the periods when DDS was switched on are counted. Then $I_{\rm bin} = N_{\rm bin}/T_{\rm bin}$ is the mean impact rate on the dust detector in the bin.
3. We calculate the mean spin-averaged sensitive area of DDS in the bin, $\bar{A}_{S\,\rm bin}$. The mean dust flux is then $F_{\rm bin} = I_{\rm bin}/\bar{A}_{S\,\rm bin}$.
4. The mean impact speed of particles, $v_{\rm bin}$, is calculated by taking the mean of the calibrated speeds of all impact events in the bin. Alternatively, one could use the expected impact speed for each population (p-, r-, a-, d-, and e-particles) instead of the mean calibrated speed. We do not make use of this approach to prevent data processing from being biased with additional theoretical assumptions. We did check, however, that it would not change the resulting number density profile significantly.
5. Finally, the number density is $n_{\rm bin} = F_{\rm bin}/v_{\rm bin}$. The error bars were calculated as

$$n^{\pm}_{\rm bin} = n_{\rm bin}\left(1 \pm \frac{1}{\sqrt{N_{\rm bin}}}\right). \tag{2}$$

When constructing a number density profile from the data in either the SDDF or DPF files, one has to keep in mind the low data transmission capability of Galileo and possible incompleteness of the data. We found the completeness factor of $AR \geq 2$ events in the region between 50 and $500R_J$ to be 100% in class 3 and $\geq$80% in the lower classes (see, e.g., Krüger *et al.* 2001). Thus, the incomplete data transmittion does not significantly affect the overall shape of the number density profile.

The whole procedure (steps 1 to 5) was performed separately for p-, r-, a-, d-, and e-particles, as well as for all particles together. The values $T_{\rm bin}$, $N_{\rm bin}$, $\bar{A}_{S\,\rm bin}$, $v_{\rm bin}$, and some others are listed in Table II. Note that the sum of the $N_{\rm bin}$'s for p-, r-, a-, d-, and e-particles is usually larger than $N_{\rm bin}$ for all particles registered, because one particle can appear in more than one of the p-, r-, a-, d-, and e-columns due to the ambiguity of the orbit determination. The number density profiles are depicted in Fig. 7 (dashed lines). The left top panel shows the overall number density in the region between $\sim 50R_J$ and $\sim 350R_J$, which is nearly flat, revealing only a slight depletion at 150–$200R_J$ and a moderate enhancement from about $200R_J$ to $350R_J$. Both the dip and enhancement are within, or at least close to, the error bars, however. The small right top panel plots the number density of grains compatible with e-orbits, illustrating that grains in very eccentric orbits could only make a minor contribution to the number density. The lower panels in Fig. 7 show again that the "partial" number density profiles determined by grains possibly in prograde, retrograde, and polar orbits look similar. We note, however, that three outermost nonzero "prograde" bins are produced by four individual events only. All these had large calibrated velocities of 9.7 km s^{-1}, hardly compatible with nearly-circular prograde orbits at the distance of detection, having orbital velocities $\approx$3 km s^{-1}. Further, three of them (events 95-304, 95-310, and 95-315 in Table I) occurred within the *JOI* orbit when the interstellar particles were approaching Galileo from nearly the same direction as prograde grains. It is likely, therefore, that at least three out of four "prograde" impacts were caused by interstellar grains rather than by the satellite ejecta. Interplanetary origin of these particles cannot be ruled out either. Thus, most of the number density between 150 and $350R_J$ seems to come from nonprograde particles.

A contamination of the data set with interplanetary and, possibly, interstellar particles mentioned before suggests that we try a somewhat stricter selection criterion. The time periods $T_{\rm bin}$ for bins between 50 and $300R_J$ vary from $\approx$130 to $\approx$750 days (Table II), 1596 days in total. We recall that the mean impact rate for interplanetary grains of masses $>10^{-11}$ g is one hit per 50 days. Therefore, for these $T_{\rm bin}$, the expected numbers of impacts of interplanetary grains with such masses are 2 to 15 per bin, with the total of 32 for all these bins. Thus, we apply the procedure above to particles with $M > 10^{-11}$ g only. With this condition, the total number of events per bin $N_{\rm bin}$ for bins between 50 and $300R_J$ is reduced from 99 to 69, but the fraction of unwanted interplanetary grains reduces to about 45%. Another reason to consider only $M > 10^{-11}$ g grains is that many of the smaller particles are lost from the data set, as they cause the $AR = 1$ impacts, which we do not analyze (see Section 2.5). The resulting histograms for grains with $M > 10^{-11}$ g only are given in the same Fig. 7 with solid lines. They indeed show that all large grains outside $150R_J$ could not have prograde orbits. Only in the inner region $r < 150R_J$ do the orbits of grains appear to include all classes—prograde, retrograde, and highly inclined ones.

A still open question is the possible presence of prograde grains in the outer zone. Galileo spent about 400 days between 150 and $350R_J$, and the mean effective sensitive area of DDS

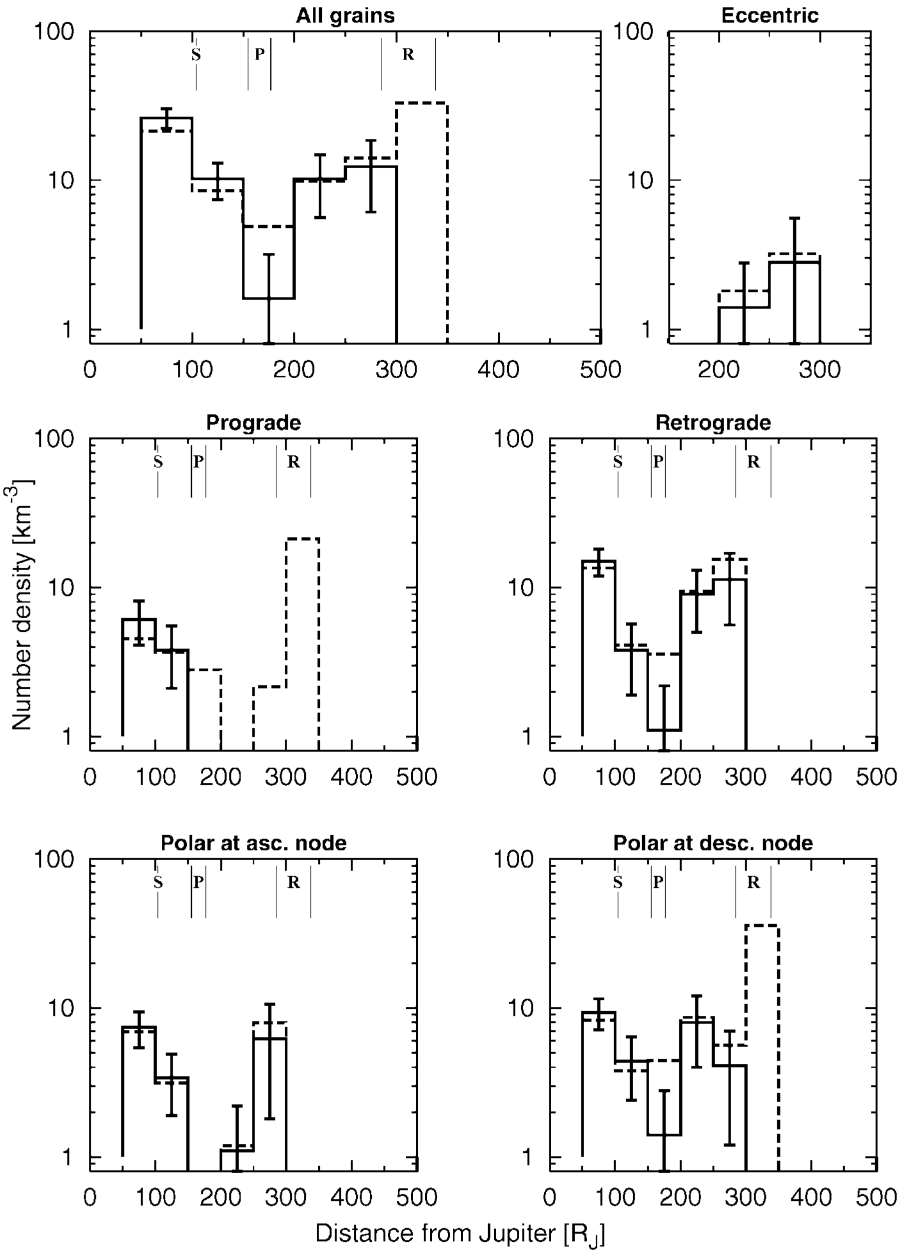

FIG. 7. Number density estimated under consideration of all dust impacts with $IA > 7$ and $v < 10\,\mathrm{km\,s^{-1}}$ (dashed lines). The histograms for events with $M > 10^{-11}$ g only are shown with solid lines (error bars are also indicated). Note that in some bins the number density of $M > 10^{-11}$ g grains is somewhat larger than of grains with all possible masses. This reflects the crudeness of the procedure of the number density derivation: it happens when the mean calibrated speed of $M > 10^{-11}$ g occurs to be smaller than that of the all grains considered, so that $n_{\mathrm{bin}} \propto N_{\mathrm{bin}}/v_{\mathrm{bin}}$ in the former case slightly exceeds n_{bin} in the latter case. Panels have the same meaning as in Fig. 6. Thin vertical lines and labels mark the orbit of S/2000J1 ("S"), the zone of 5 prograde moons ("P"), and the region of 14 retrograde moons ("R").

with respect to grains in both retrograde and polar orbits was about three times as large as that for prograde grains (Table II). Consequently, if the number densities of prograde and retrograde dust in this region were comparable, about three times fewer prograde particles would be detected than retrograde or highly inclined ones. The actual numbers in the data set are 4 and 18, respectively. If only $M > 10^{-11}$ g grains are counted, we get 0 and 10 events, respectively. Therefore, the dominance of the retrograde orbits is likely. Measurements in future *I33* and especially *A34* orbits would be useful to check this.

2.8. *Pioneer and Ulysses Data*

So far we have discussed the data obtained by the Galileo spacecraft. Apart from Galileo, three other spacecraft equipped with dust detectors have flown through the jovian system:

TABLE II
Distribution of Impact Events with $IA > 7$ and $v < 10$ km s^{-1} in Distance Bins

Distance bin $[R_J]$	T_{bin} [days]	S/c mean speed [km s^{-1}]	v_{bin} [km s^{-1}]						$\bar{A}_{S\mathrm{bin}}$ [cm^2]						N_{bin}					
			all	p	a	r	d	e	all	p	a	r	d	e	all	p	a	r	d	e
50 100	753	3.6	3.8	4.5	3.8	3.6	3.6	3.8	116	113	121	108	121	96	61	14	19	32	22	32
100 150	447	2.1	4.8	5.1	4.9	2.2	4.8	2.0	120	104	125	126	125	102	19	7	7	4	8	4
150 200	135	1.9	5.8	9.7	0.0	4.5	4.5	0.0	122	34	140	172	140	151	4	1	0	3	3	0
200 250	129	1.4	4.9	0.0	6.4	4.9	3.4	7.1	110	52	131	125	132	143	6	0	1	6	4	2
250 300	132	0.7	4.1	9.7	2.7	3.2	5.2	5.4	106	45	131	115	132	155	7	1	3	6	4	3
300 350	6	6.5	9.7	9.7	0.0	0.0	9.7	0.0	121	202	120	41	120	120	2	2	0	0	2	0
350 400	7	6.4	0.0	0.0	0.0	0.0	0.0	0.0	123	201	122	45	123	122	0	0	0	0	0	0
400 450	7	6.3	0.0	0.0	0.0	0.0	0.0	0.0	124	199	124	51	124	124	0	0	0	0	0	0
450 500	6	6.2	0.0	0.0	0.0	0.0	0.0	0.0	126	199	126	54	126	126	0	0	0	0	0	0

Note. See Section 2 for notation.

Pioneer 10 and 11 in 1973–1974 and Ulysses in 1992. The Pioneers carried arrays of pressurized cells, acting as low-sensitivity dust detectors with the threshold of about 10^{-9} to 10^{-8} g, or about 10 μm in terms of sizes. Although they did detect a dozen of meteoroid impacts inside $\approx 50 R_J$ (Humes 1976), the sensitivity was far too low, and the flyby time too short, to detect any events in the outermost part of the jovian system.

Ulysses, equipped with the same dust detector as Galileo, made a flyby of Jupiter in 1992. We processed the Ulysses flyby data set in a similar way to Galileo's, with the only difference that a weaker speed criterion $v < 20$ km s^{-1} was used. The reason for that is the large speed of the spacecraft itself, $\approx$15 km s^{-1}, so that larger impact speeds of bound particles could be expected. We note, however, that weakening the speed criterion has a danger of increasing the fraction of interstellar grain impacts in the data set. Seven impacts occurred between 59 and $466 R_J$, of which one or two may have been ejecta from retrograde outer moons, while the others were most likely interstellar grains.

3. THEORY

3.1. Dust Production by Outer Satellites

Six tiny outer moons orbit Jupiter in prograde and fourteen in retrograde orbits (Table III). As with all other bodies in the Solar system that lack an atmosphere, these irregular jovian satellites are expected to be sources of dust through hypervelocity impacts of interplanetary micrometeoroids. Recent in-situ measurements by Galileo have led to the discovery of impact-generated dust clouds around the Galilean moons of Jupiter (Krüger *et al*. 1999c, 2000). These detections demonstrated the efficiency of the impact ejecta production via micrometeoroid bombardment. Furthermore, the Galileo data turned out to be consistent with our model of an impact-generated dust cloud around a moon (Krüger *et al*. 2000). Here we apply exactly the same model, tested on the Galilean moons, to the outer satellites.

Using Divine's (1993) model, Krüger *et al*. (2000) calculated the mass flux of interplanetary micrometeoroids onto a sphere with a unit cross section, moving around the Sun in a circular Keplerian orbit with a radius of 5.2 AU (heliocentric distance of Jupiter): $F_{\mathrm{imp}} \approx 10^{-16}\,\mathrm{g\,cm^{-2}\,s^{-1}}$. The average speed of the projectiles with respect to Jupiter was estimated as $v_{\mathrm{imp}} \approx 20\,\mathrm{km\,s^{-1}}$.

We now consider the impact ejecta production. The mass production rate of the escaping ejecta from the satellite surfaces is

$$M^+ = F_{\mathrm{imp}} Y \sum_A S_A \Phi_A. \tag{3}$$

Here, Y is the characteristic yield, defined as the ratio of the ejected mass to the projectile mass; $S_A = \pi R_A^2$ is the cross section area of a satellite A ($R_A =$ its radius); Φ_A is the fraction

TABLE III
Outer Jovian Satellite Data[a]

Satellite(s)	a $[R_J]$	e	i [deg]	Radius [km]
Prograde satellites				
S/2000J1	104	0.20	46	4
Leda	156.3	0.16	27.46	5
Himalia	160.5	0.16	27.50	85
Lysithea	164.2	0.11	28.30	12
Elara	164.4	0.22	26.63	40
S/2000J11	177	0.22	29	2
Retrograde satellites				
Ananke	298.0	0.24	148.89	10
Carme	327.7	0.25	164.91	15
Pasiphae	330.8	0.41	151.43	18
Sinope	335.3	0.25	158.11	14
S/2000J2–S/2000J10	285–338	0.16–0.53	146–166	2–3

[a] Mean orbital elements of eight "classical" moons from Jacobson (2000), their radii from Murray and Dermott (1999); all data for newly discovered satellites from Sheppard *et al*. (2000, 2001).

of escaping ejecta among all grains ejected from the surface. The yield is known to depend on the mechanical properties of the target material, target mass, as well as on the masses and speeds of the projectiles. Assuming regolith-like targets (a plausible choice for jovian irregulars that resemble C- and D-type asteroids; see Sykes *et al.* 2000), impact speeds of $\approx$20 km s^{-1}, and a characteristic impactor mass of 10^{-5} g, the yield is $Y \approx 10^3$ (D. Koschny, pers. comm.). Simple estimates show that nearly all ejecta from the satellites escape: $\Phi_A \sim 1$. The only exception is the largest of the satellites, Himalia (radius 85 km). Assuming a reasonable ejecta speed distribution with the slope 1.2 and the minimum ejecta speed 60 m s^{-1} (Krüger *et al.* 2000), we get $\Phi_A \sim 0.5$ for this moon, giving $\sum_A S_A \Phi_A \sim 6 \times 10^{13}$ cm^2 for the prograde satellites (dominated by Himalia) and $\sim 2 \times 10^{13}$ cm^2 for the retrograde family. Now, Eq. (3) gives $M^+ \sim 6$ g s^{-1} and $\sim$2 g s^{-1}, respectively.

The number of particles with masses $>M$ ejected from the moon per second is [Eq. (3) of Krüger *et al.* 2000]

$$N^+(>M) = \frac{1-\alpha}{\alpha} \frac{M^+}{M_{\max}} \left(\frac{M_{\max}}{M} \right)^{\alpha}, \tag{4}$$

where M^+ is given by (3), $M_{\max} \sim 10^{-5}$ g is the largest mass of the ejecta, and $\alpha \sim 0.8$ is the slope of the cumulative mass distribution of the ejecta. Numerically, $N^+(>10^{-13}\text{ g}) \sim 4 \times 10^{11}$ s^{-1} for the prograde family and $N^+(>10^{-13}\text{ g}) \sim 1 \times 10^{11}$ s^{-1} for the retrograde group. For $M > 10^{-11}$ g, the values are $\sim 9 \times 10^9$ s^{-1} and $\sim 3 \times 10^9$ s^{-1}, respectively. The uncertainty of these estimates is at least one order of magnitude (see Section 3.7).

3.2. *Equations of Motion*

We now discuss the ejecta dynamics. Simple estimates show that two perturbing forces dominate the dynamics that far from the planet: solar tidal gravity and, for grains smaller than $\sim 100\,\mu$m, solar radiation pressure. Later we shall see that time scales involved are long enough to make a dissipative force, the Poynting–Robertson force, also important. Finally, most of the time dust grains move outside the jovian magnetosphere, where they are directly exposed to the solar wind, and can occasionally cross the magnetotail of Jupiter, experiencing the planetary magnetic field. In both cases, the particles will be subject to the Lorentz force, which may have dynamical consequences for submicrometer-sized motes—see, e.g., Horányi *et al.* (1990, 1991) (interaction with the solar wind) and Hamilton and Krivov (1996) (jovian magnetic field). The Lorentz force is not considered here, so our results for such grains should be taken with caution.

We start with the first two forces. To describe them, Hamilton and Krivov (1996) introduced two dimensionless parameters. The radiation pressure parameter C is defined as

$$C \equiv \frac{3}{2} \frac{n}{n_\odot} \sigma, \tag{5}$$

where n and $n_\odot$ are mean motions of the grain about the planet and the planet about the Sun, respectively, and σ is the ratio of the radiation pressure to planetary gravity force for a grain at a distance a from the planet:

$$\sigma = \frac{3}{4} Q_{pr} \frac{F_\odot a^2}{\mu c \rho_g r_g}. \tag{6}$$

Here, Q_{pr} is the radiation pressure efficiency factor, $F_\odot$ is the solar flux at the heliocentric distance of the planet, μ is the gravitational parameter of the planet, c is the speed of light, and r_g and ρ_g are the radius and bulk density of the grain assumed to have a spherical shape. The solar tidal force parameter A is given by

$$A \equiv \frac{3}{4} \frac{n_\odot}{n}. \tag{7}$$

In orbit-averaged approximation, in 2D case (prograde with inclination $i = 0°$) and under some simplifying assumptions (circular orbit of the planet, absence of a planetary shadow, etc.), Hamilton and Krivov (1996) have shown that the grain semimajor axis has no secular change, and that the eccentricity e and the solar angle $\phi_\odot$ (the angle between the directions from the planet to the Sun and to the pericenter of the grain orbit) obey the equations

$$\frac{de}{d\lambda_\odot} = -\frac{\sqrt{1-e^2}}{e} \frac{\partial \mathcal{H}}{\partial \phi_\odot}, \quad \frac{d\phi_\odot}{d\lambda_\odot} = \frac{\sqrt{1-e^2}}{e} \frac{\partial \mathcal{H}}{\partial e}, \tag{8}$$

where $\lambda_\odot$ is the longitude of the Sun (a linear function of time) and $\mathcal{H}$ is the conserved Hamiltonian,

$$\mathcal{H} = \sqrt{1-e^2} + Ce\cos\phi_\odot + \frac{1}{2} A e^2 [1 + 5\cos(2\phi_\odot)]. \tag{9}$$

This work was extended by Hamilton and Krivov (1997), who considered a modification of the approach to retrograde orbits, perturbed by the solar tidal gravity only. Inclusion of radiation pressure is straightforward: for inclinations $i = 180°$, the Hamiltonian (9) transforms to

$$\mathcal{H} = -\sqrt{1-e^2} + Ce\cos\phi_\odot + \frac{1}{2} A e^2 [1 + 5\cos(2\phi_\odot)]. \tag{10}$$

3.3. *Dust Dynamics: Analytic Study*

The dynamics of particles ejected from different moons within either group are expected to be similar because of the similarity of the satellites' orbital elements. The only exception is the innermost irregular S/2000J1 which, however, makes little contribution to the overall ejecta cloud because of its small size. To analyze the ejecta dynamics, we therefore choose one

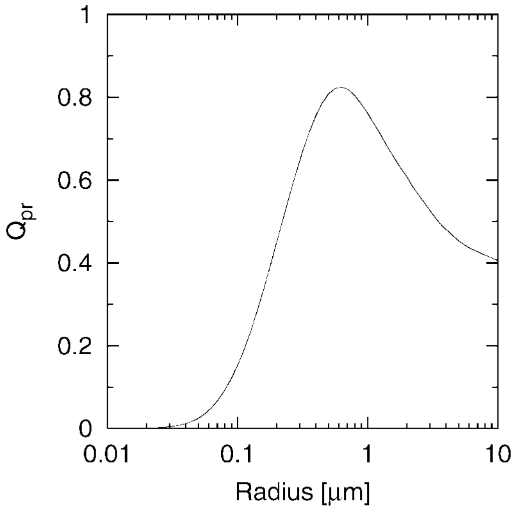

FIG. 8. Radiation pressure efficiency of the material adopted in the calculations of the radiation pressure force.

source satellite in each group: Himalia, the largest of the prograde moons, and Carme, one of the retrograde satellites. For Himalia, $C = 1.43 Q_{pr}(r_g)(1\ \mu\text{m}/r_g)$ and $A = 0.043$, whereas for Carme $C = 2.05 Q_{pr}(r_g)(1\ \mu\text{m}/r_g)$ and $A = 0.126$.

To calculate the radiation pressure efficiency Q_{pr}, we choose one of the silicates, a dielectric material with less absorption in visible light (for its parameters; see Kimura *et al.* 1997, Krivov *et al.* 1998). The radiation pressure efficiency Q_{pr} as a function of particle's radius is plotted in Fig. 8. The bulk density is $\rho_g = 2.37\ \text{g cm}^{-3}$.

The phase portraits in polar coordinates $e \cos \phi_\odot$ and $e \sin \phi_\odot$ resulting from Eqs. (8) with the Hamiltonians (9) and (10) are depicted in the left and right valves of Fig. 9, which correspond to Himalia and Carme, respectively. Thick lines in panels from top to bottom are lines of the constant Hamiltonian for particles with sizes 5.0, 2.0, and 1.4 μm. Two curves are depicted in each of the panels: those with initial solar angles of $\phi_{\odot 0} = 0°$ and $\phi_{\odot 0} = 180°$.

The basic features of the dynamics, as seen in Fig. 9, are as follows. Firstly, the prograde trajectories are elongated in the Sun–planet direction and the maximum eccentricities are attained when the solar angle is zero; the retrograde orbits are elongated in the direction perpendicular to the Sun–Jupiter line and the eccentricities reach maximum when the solar angle is between 90° and 180°. This directly translates to the geometry of the dust rings formed by the prograde and retrograde satellite ejecta. The prograde ejecta cloud is elongated in the solar direction and is shifted away from the Sun while the retrograde cloud is more extended in the perpendicular direction and is offset toward the Sun (Fig. 11 below).

Second, regardless of the sense of the orbital motion, the maximum eccentricity $e_{\max}$ increases with the parameter C, i.e., with increasing radiation pressure strength. The parameter C tends to zero for both $r_g \to 0$ and $r_g \to \infty$ and has a maximum value of 3.30 (4.74) for Himalia (Carme) at $r_g \approx 0.22\ \mu$m. For particles $\gg 1\ \mu$m, $C \ll 1$ and $e_{\max} \ll 1$; the orbits are stable. At a certain critical radius, $r_g \approx 1\ \mu$m, both C and $e_{\max}$ approach unity. Along with the fact that the semimajor axis remains nearly constant, this means that the grains hit Jupiter in about one jovian year (1 j.y. $\approx$ 12 years). Interestingly, the critical size is about 1 μm for both retrograde moons and the prograde ones. Although the retrograde orbits are known to be more stable against solar tidal gravity and radiation pressure than their prograde cousins (see, e.g., Hamilton and Krivov, 1997), this is counterbalanced by the fact that prograde moons are orbiting closer to the planet where both perturbations are weaker.

For grains with sizes below the critical one, $r_g \lesssim 1\ \mu$m, the radiation pressure perturbations become so strong that the

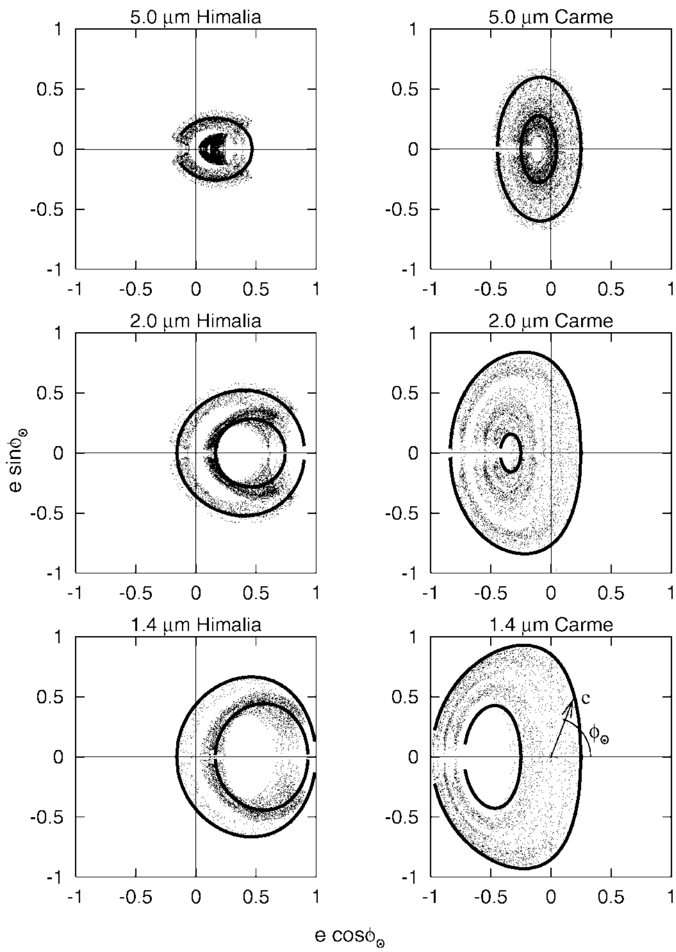

FIG. 9. Phase portraits for different-sized grains ejected from prograde Himalia (left) and retrograde Carme (right). Dots are numerical integration results—10 trajectories with randomly chosen $\phi_{\odot 0}$, grain's longitude of the ascending node, and its initial mean anomaly. Two curves in each panel are analytic lines of the constant Hamiltonian for $\phi_{\odot 0} = 0°$ and 180°, which nearly bracket the numerically-integrated trajectories. The avoidance of regions $\phi_\odot \approx 0°$ and 180° by numerical integration dots, distinctly seen in the left panels, arises from three-dimensionality of the problem (non-zero inclinations). The effect disappears when a 2D problem is numerically integrated.

orbit-averaging approximation breaks down. Further, the problem becomes essentially three-dimensional because the orbital inclinations are strongly perturbed. To see whether some of these grains are still able to keep in bound orbits over sufficiently long time intervals, we will employ numerical integration (see below). We note that for *very* small grains the parameter C becomes small again: for instance, the 0.06-μm grains have the same C as the 1 μm ones. Formally, the analytic theory applies to such tiny motes, as it does for micrometer-sized ones. However, various erosion mechanisms make their lifetimes too short for them to contribute significantly to the dust complex. Besides, such grains are far below the Galileo DDS threshold for the impact speeds of several km s^{-1}, and so were not detected anyway.

Thirdly, the trajectory of a particular grain depends on the initial conditions (e_0, $\phi_{\odot 0}$). The trajectories shown as lines in Fig. 9 are computed for $e_0 = 0.16$ and 0.25 (Himalia's and Carme's eccentricity) and for two initial solar angles: $\phi_{\odot 0} = 0°$ and 180°, which represent two limiting cases. In the prograde case, the grains ejected at $\phi_{\odot 0} = 180°$ have the largest maximum eccentricities, and those with $\phi_{\odot 0} = 0°$, the smallest ones. The retrograde case shows the reverse. This means that the critical radius depends on the initial solar angle. For example, smaller grains from a prograde moon can survive, if they are ejected at the moment when the pericenter of the satellite orbit looks toward the Sun.

3.4. *Dust Dynamics: Numerical Simulations*

Having useful guidelines from the analytic theory, we then performed numerical integrations of the more realistic—nonaveraged, three-dimensional—problem. The equations of motion in cartesian coordinates, taking into account the jovian gravity, radiation pressure, solar tidal gravity, and Poynting–Robertson effect were integrated by Everhart's (1985) method of 9th order with a variable time step over the time interval up to 50,000 j.y. $\approx 6 \times 10^5$ years. Particles of several sizes between 5.0 and 0.1 μm were launched from Himalia and Carme. For either moon and each size, up to 20 trajectories with randomly generated initial solar angle $\phi_{\odot 0} \in [0°, 180°]$, grain's mean anomaly, and longitude of ascending node were integrated.

As expected from the theory, all particles with sizes $r_g > 1\ \mu$m stay in bound orbits over the whole integration interval. The semimajor axis is nearly constant on short time scales; over a longer time interval, it experiences a gradual decrease due to the Poynting–Robertson effect. The behavior of e and $\phi_\odot$ also follows the analytic expectations very well. The results are plotted in Fig. 9 with dots. Although the numerically integrated points are scattered appreciably, they are indeed nearly bracketed with the two analytically-found lines of the constant Hamiltonian for $\phi_{\odot 0} = 0°$ and $\phi_{\odot 0} = 180°$.

What happens to smaller grains? All integrated trajectories of 1.0 μm and smaller grains from the retrograde Carme do not survive over the integration interval of 50,000 j.y.—most of them are already lost in about 1 j.y. So do all 1.0, 0.7, and 0.1 μm grains from the prograde Himalia—only some of the Himalia ejecta survived up to 1,000 j.y. The grains with r_g from 0.2 to 0.5 μm from Himalia are surprisingly more stable. About 10 to 20% of these survive over 10,000 j.y. and thus may markedly contribute to the dust complex. Remember, however, that the actual behavior of these tiny motes may be more complex because of the Lorentz force, which is not included in our model.

Another important issue is perturbations in the orbital planes. As the 2D analytic theory presented above is no longer applicable, we use numerical integration. Figure 10 depicts inclination histories of grains with sizes from 2.0 down to 0.3 μm. The grains with radii just above 1 μm from both prograde and retrograde moons are already perturbed strongly enough to get in polar orbits. Furthermore, the submicrometer-sized particles from prograde moons, if they survive, are perturbed so strongly that not only polar, but also retrograde orbits become quite common.

3.5. *Spatial Distribution of Dust*

To determine the spatial distribution of dust, we used the numerical runs described above. Instantaneous positions of grains were stored with the printout step of 1 j.y. The resulting scatter plots are shown in Fig. 11. As in Fig. 10, left and right columns are for Himalia and Carme, respectively. Panels from top to bottom are for 2.0-, 1.4-, 0.5-, and 0.3-μm-sized grains. The coordinate system is the jovicentric equatorial one, with x-axis pointing to the Sun. It is the same as in Fig. 3, allowing direct visual comparison with the DDS impact events. Note that we have only plotted the grain positions located near the equatorial plane of Jupiter, namely in the latitudinal belt of $\pm 5°$. This is done because we are going to compare the modeling results with the dust detections of Galileo, which has been orbiting Jupiter nearly in the equatorial plane.

The left column plots clearly show that many ejecta from prograde moons are expected on the anti-solar side of Jupiter, coincidentally in the region sampled by many Galileo orbits during the middle phase of the mission. Ejecta from retrograde satellites are more scattered in space; dust from the retrograde sources could be expected in most of the Galileo locations during its orbital tour.

3.6. *Loss Mechanisms and Grain Lifetimes*

Many of the submicrometer-sized grains from prograde moons are lost because the combined radiation pressure and solar gravity perturbations force them to enter the innermost part of the jovian system or even hit the planet. The time scales involved have already been discussed.

Consider now other possible loss mechanisms, which are especially important for the particles that get in stable orbits about Jupiter (e.g., all grains with $r_g > 1\ \mu$m). A universal loss mechanism is the Poynting–Robertson effect. The time it takes for a grain to reduce its semimajor axis from a_0 to a_1 due to

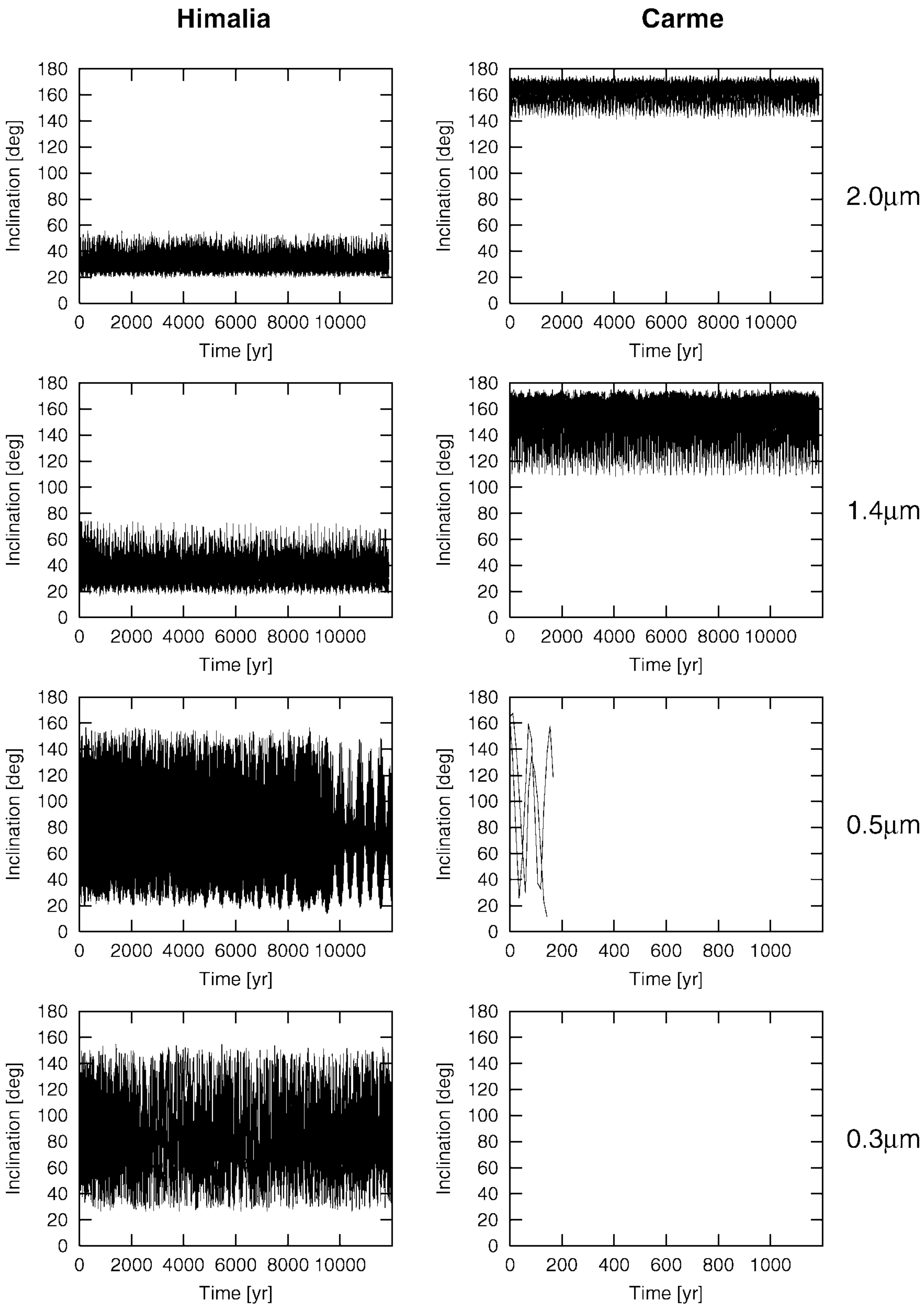

FIG. 10. Numerically simulated evolution of the orbital inclination of the 2.0, 1.4, 0.5, and 0.3 μm-sized grains ejected from prograde Himalia (left) and retrograde Carme (right). The initial inclinations are those of the parent moons—27.5° and 164.9°, respectively. The submicrometer-sized particles from the retrograde Carme are absent—they are quickly lost to the radiation pressure perturbations. The panel for 0.5 μm Carme grains (note a different time scale) shows the only one of 10 particles that survives longer than 1 j.y. All simulated 0.3 μm Carme grains were eliminated by the radiation pressure in less than 1 j.y. Intermediate-sized grains (1.0 and 0.7 μm) are not plotted because they are rapidly removed.

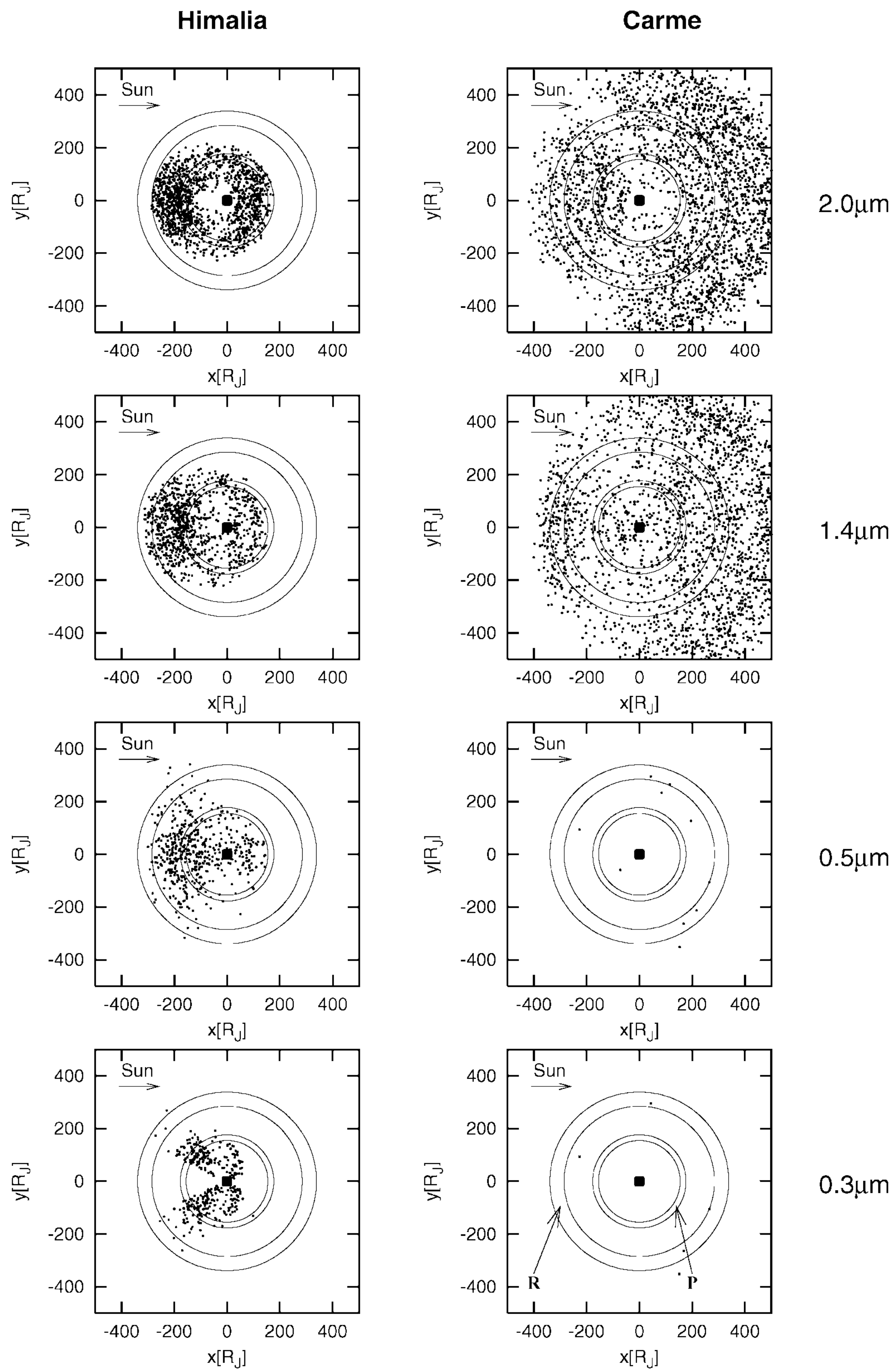

FIG. 11. Scatter plots for the same grains as in Fig. 10. The panels for submicrometer-sized Carme grains are nearly empty, because these are rapidly lost. Two pairs of circles mark the region of 5 prograde ("P") and 14 retrograde ("R") moons.

Poynting–Robertson drag is (e.g., Burns *et al.* 1979)

$$T_{PR}(a_0, a_1) = \tau_{PR} \ln(a_0/a_1), \tag{11}$$

where τ_{PR} is the exponential decay time,

$$\frac{\tau_{PR}}{1\,\mathrm{yr}} = \frac{5.6\times10^3}{5+\cos^2 i}\left(\frac{R}{1\,\mathrm{AU}}\right)^2 \times \left(\frac{\rho}{1\,\mathrm{g\,cm^{-3}}}\right)\left(\frac{r_g}{1\,\mu\mathrm{m}}\right)\left(\frac{1}{Q_{pr}}\right), \tag{12}$$

with $R = 5.2$ AU being the heliocentric distance of Jupiter. Taking a_0 from Table III and putting $a_1 = 1R_J$, we find for a 0.2 μm-sized silicate particle from Himalia, for instance, $T_{PR} \approx 1 \times 10^5$ yr, whereas for a 1 μm-sized grain from Carme $T_{PR} \approx 5 \times 10^5$ yr. On these time scales, the grains will be brought into the inner jovian system where they will swiftly be lost.

Let us consider other possible sinks. Collisions with a parent satellite or other outer moons are inefficient. Simple "particle-in-a-box" estimates give typical collision times as $>10^9$ years (!), which is not surprising, because the largest of the outer moons, Himalia, is only 85 km in radius, whereas the spatial volume filled in by the grains, is huge: $\sim10^{22}$ km^3. The lifetime against collisions with interplanetary or interstellar grains is $\sim10^5$ to 10^6 years (Burns *et al.* 1984). Sublimation can be important for pure icy grains only; for realistic albedos, the timescale is very long—$\sim10^7$ years (Burns *et al.* 1984). Electrostatic bursting is also inefficient. The complete fracture of grains due to this mechanism is improbable even in the much more severe environment closer to Jupiter; see Burns *et al.* (1980). Gradual erosion through removing tiny surface asphericities from a grain is possible, but the related erosion times are likely to be very long. The same applies to sputtering by solar wind and jovian magnetotail ions.

3.7. *Expected Number Densities*

We now make a ballpark estimate of the number density that could be expected in both prograde and retrograde dust populations. Consider the $M > 10^{-11}$ g or $r_g > 1\,\mu$m grains only. The mean number density is

$$n \sim N^+ T/V. \tag{13}$$

Here, $N^+ = N^+(>10^{-11}\,\mathrm{g})$ is the production rate ($\sim 9\times10^9\,\mathrm{s^{-1}}$ for prograde moons and $\sim3\times10^9\,\mathrm{s^{-1}}$ for retrograde ones; see Section 3.1), T is the typical lifetime of the grains in jovian space, and V is the volume of the dust complex. The volumes occupied by the two populations (see Fig. 11) are estimated as $V \sim 8\times10^{21}$ km^3 and $V \sim 3\times10^{22}$ km^3, respectively. The lifetimes (Eqs. 11 and 12) are $T \sim T_{PR} \approx 4\times10^5$ yr and $\approx 5\times10^5$ yr. The number density is then $n \sim 15\,\mathrm{km^{-3}}$ for the debris of the prograde moons and $n \sim 1\,\mathrm{km^{-3}}$ for those of the retrograde satellites.

We emphasize that these estimates are *very* rough. Most of the uncertainty comes from that of the factor $Y\Phi_A$ in Eq. (3) (about 1 order of magnitude; see Section 6.1 of Krivov and Banaszkiewicz 2001) and that of the factor T/V in Eq. (13) (probably about one order of magnitude as well). Besides, other parameters in Eqs. (3) and (4), such as F_{imp}, could be uncertain by a factor of several (0.5 orders of magnitude). Assuming the logarithms of $Y\Phi_A$, T/V, and F_{imp} to be statistically independent, normally distributed random variables with variances of 1, 1, and 0.5, respectively, the logarithm of their product (and therefore $\log n$) is then a random variable with a standard deviation $\sqrt{1^2+1^2+0.5^2} \approx 1.5$. Thus, the resulting number density n is uncertain at least by a factor of 30—perhaps even more, as the assumptions of the model, e.g., power-law mass distribution of the ejecta, are only approximations to the reality.

4. DATA VS THEORY

Our analysis of the Galileo DDS data (Section 2) suggests the presence of a previously unknown population of dust particles between about 50 and $350R_J$. A natural source for these grains would be outer small jovian satellites—both prograde moons at $\approx150R_J$ and retrograde ones at $\approx300R_J$. In an attempt to check this, we investigated the production, dynamics, sinks, and distributions of such ejecta theoretically (Section 3). We now make a detailed comparison of the properties of dust derived from the data with those resulting from our theoretical analysis.

4.1. *The Number Density Profile*

The number density of micrometer-sized particles derived from the data between 50 and $350R_J$ has a nearly constant level of $n \sim 10\,\mathrm{km^{-3}}$ (with a factor of 2 or 3 uncertainty) and sharply drops down outside $350R_J$ (Fig. 7). The very fact that the number density drops down at $350R_J$ is not compatible with "external" (interplanetary or interstellar) origin, and there are additional arguments against this interpretation. The number density of interplanetary particles can be estimated from the Galileo measurements just before the spacecraft entered the jovian system. In Section 2.5 we found the impact rate of $>10^{-11}$ g interplanetary grains onto the DDS to be about one hit per 50 days. Assuming a $20\,\mathrm{km\,s^{-1}}$ speed and an average sensitive area of $100\,\mathrm{cm^2}$, this translates to $n_{IP} \sim 1\,\mathrm{km^{-3}}$, close to what Divine's (1993) model gives. Like-massed interstellar grains ($>10^{-11}$ g) have the average flux $1\,\mathrm{km^{-2}\,s^{-1}}$ (Landgraf *et al.* 2000), thus their number density is much smaller, $n_{IS} \lesssim 0.1\,\mathrm{km^{-3}}$. Besides, nearly all interstellar grains should be faster ($\approx 26\,\mathrm{km\,s^{-1}}$) than the grains we selected ($<10\,\mathrm{km\,s^{-1}}$). In addition, interstellar motes were not always detectable. For instance, in 2000–2001 (the orbits *G28* and *C29*) the interstellar grains approached Jupiter essentially from the solar direction and, like prograde circumjovian particles, could not be detected by the Galileo DDS.

On the other hand, our theoretical estimates show that the $10\,\mathrm{km^{-3}}$ level is quite compatible with the hypothesis of the impact-generated outer satellite ejecta. As the uncertainties of such estimates are extremely high, we stress that these are merely compatibility estimates and do not provide evidence for the satellite origin of the detected grains.

4.2. *The Mass Distribution*

The mass distribution of the selected grains is unusual, showing that the mass regime around 10^{-11} g (or about 1 μm in radius for the material density of $\approx 2\ \mathrm{g\,cm^{-3}}$) is devoid of dust (Fig. 5, bottom). This is not typical of interplanetary (Divine 1993) and interstellar grains (Landgraf *et al*. 2000), both having smooth, nearly power-law distributions in the mass regime under study. This is directly supported by our analysis of the "background dust" (Fig. 5, top). Therefore, we argue that the peak on the right of the bottom panel in Fig. 5 is produced by outer satellite ejecta.

And indeed, the derived mass distribution is consistent with the simulated dynamics of the ejecta from the outer jovian moons. Although the calculations have been made for one type of silicate, we speculate that such a behavior is generic for many materials. We have shown that all ejecta from both prograde and retrograde moons with sizes $\gtrsim 1\ \mu$m are in stable orbits, producing the peak on the right of the bottom panel in Fig. 5. Furthermore, our simulations suggest that some of the ejecta of prograde satellites with sizes 0.2–0.5 μm can also stay in planetocentric orbits for sufficiently long time intervals. This might explain, at least in part, the peak on the left of the bottom panel in Fig. 5. This conclusion is not certain, however: this peak can also largely be attributed to interplanetary/interstellar dust (see top panel in Fig. 5).

4.3. *The Spatial Distribution*

Most of the dust impacts selected from the data set (78 out of 99 events) occurred in the "middle phase" of the mission (orbits *G1* to *I27*) when Galileo densely covered the distance range 50–150R_J on the antisolar side from Jupiter (Fig. 3). This is exactly the region where the ejecta from the outer prograde moons are expected to dominate the dust environment (Fig. 11, left panels). DDS was sensitive, on the average, to all orbit types. Accordingly, all types of orbits and all masses are equally present. This agrees with the theory: a lot of small and large ejecta from prograde moons are expected there with all types of orbits (Fig. 10, left panels). A small fraction of the events could have been caused by ejecta from retrograde moons (Fig. 11, right panels).

The detections near the apojoves of the later orbits *G28* and *G29* (last 12 events in Table I) can be attributed to the debris lost by outer retrograde satellites. These detections took place at 150–300R_J and appear in the upper part of Fig. 3. DDS was sensitive to retrograde and polar grains and detected both. Grains near apocenters of highly eccentric orbits, whether prograde, retrograde, or polar, could be detected as well, but a fraction of such grains in the data set is low. All detected grains but one had calibrated masses $>10^{-12}$ g, with 9 out of 12 events having masses $>10^{-11}$ g. All these facts are consistent with the theory: large grains in nonprograde, moderately eccentric orbits from retrograde moons are expected there.

That no impacts between 500 and 350R_J occurred during the initial *JOI* leg does not contradict the theory: the region can only contain ejecta from retrograde moons, which are present with lower number densities and are moving in nonprograde orbits. On the other hand, Galileo spent only 20 days there. A comparison with the detections made between 200 and 300R_J (Table II) shows that 20 days is about the time during which one impact occurs. Furthermore, between 500 and 350R_J DDS could only detect polar, but not retrograde, particles, so that even a single impact there could not necessarily be expected.

Another fact that needs to be explained is nondetection of dust satisfying our criteria during the second half of the *J0* orbit, after the apojove (DDS was switched off before). Since DDS was sensitive to prograde grains only, this is understandable: grains from prograde moons are not expected in this region (Fig. 11, left), while grains from retrograde sources could be there (Fig. 11, right), but cannot be prograde (Fig. 10, right).

Thus, the majority of the events can be explained. We stress, however, that an exact interpretation of any individual event is not possible. In most cases, we can only argue that a detected grain is compatible with having a satellite origin, but cannot rule out a possibility of an interplanetary (sometimes also an interstellar) particle impact.

4.4. *The Distribution of the Orbital Inclinations*

Our analysis of the Galileo DDS data shows that in the inner region $50R_J < r < 150R_J$ the orbits appear to include all classes—prograde, retrograde, and highly inclined ones—whereas most of the number density between 150 and 350R_J seems to come from nonprograde particles (Fig. 7, solid histograms). This agrees with the identification made above—grains from prograde moons in the inner region and from the retrograde ones in the outer region. We have argued that the former can easily be transformed by the radiation pressure from prograde to polar and retrograde orbits, whereas the latter are excluded from prograde orbits (see Fig. 10).

5. CONCLUSIONS

This paper provides a study of the dust environment in the outer region of the jovian system outside the orbits of the Galilean satellites—between ~50 and 500 jovian radii from the planet. The study includes an analysis of in-situ measurements by the dust detector aboard the Galileo spacecraft, theoretical modeling, and a comparison between them. Our main findings can be summarized as follows.

1. About 100 individual events in the Galileo data set are fully compatible with being caused by impacts of micrometer-sized grains moving about Jupiter in bound orbits with moderate

eccentricities and very different inclinations—from prograde to retrograde ones. We thus argue for the presence of a previously unknown population of dust particles between about 50 and $300 R_J$. A number of properties of this dust population have been established. The calibrated speeds of dust grains in question (several km s^{-1}) are compatible with bound circumjovian orbits. The mass distribution of the selected grains was found to have a gap around 10^{-11} g (or about 1 μm in radius for the material density of $\approx$2 g cm^{-3}). The radial profile of dust number density is nearly flat between about 50 and 300 jovian radii, with the absolute number density level of $\sim$10 km^{-3} (uncertain by a factor of 2 or 3). This is by two orders of magnitude less than the density of dust near the Europa orbit and by a factor of 10 less than the dust density at Callisto's orbit ($\sim 10^3$ km^{-3} and $\sim 10^2$ km^{-3}, respectively; see Krivov *et al.* 2002), yet an order of magnitude more that in the nearby interplanetary space.

2. Large distances from Jupiter rule out a number of sources/ mechanisms known to act in the inner jovian system: electromagnetically captured interplanetary dust (Colwell *et al.* 1998); dust from the Galilean (Krivov *et al.* 2002) or small inner (Burns *et al.* 1999) satellites; dusty "traces" of the SL9 comet's impact (Horányi 1994). Our events were observed mostly in the second amplitude range of the Galileo DDS that drastically minimizes the probability of stream particle impacts. The impacted grains had speeds of several km s^{-1}, which excludes interstellar particles. We suggest that these grains derive from outer small jovian satellites. Impacts by interplanetary micrometeoroids onto their surfaces create ejecta, nearly all of which get injected to the circumjovian space. The subsequent dynamics are controlled by solar tidal gravity and radiation pressure and, on longer time scales, by Poynting–Robertson drag. Our analytic and numerical study of the ejecta dynamics shows that micrometer-sized particles from both prograde and retrograde satellite families and a nonnegligible fraction of smaller ejecta from prograde moons would remain in bound orbits for hundreds of thousands of years. This implies a mass distribution consistent with the one derived from the data, with a gap around 10^{-11} g. The micrometer-sized grains from both groups of sources can develop significant inclinations, reaching polar orbits. Submicrometer-sized dusty survivors from prograde moons find themselves in all types of orbits—prograde, polar, and retrograde ones. Different-sized ejecta from both families of satellites form spheroidal clouds embracing the orbits of the parent moons, with appreciable asymmetries.

3. The number density profiles, mass distribution, sense of the orbital motion of dust, as well as radial and azimuthal distribution of the impacts derived from the data analysis are largely consistent with the dynamical model. Most of the dust impacts in the "middle phase" of the mission (orbits *G1* to *I27*) are well explained by impacts of the ejecta from the outer prograde moons, while the detections near the apojoves of the later orbits *G28* and *G29* can be successfully attributed to the debris lost by outer retrograde satellites. We have also shown that, although an appreciable fraction of individual impacts that may have been caused by interplanetary and interstellar grains and, in some cases, also jovian stream particles, these sources alone fail to explain the data.

A further study of the dust structures on the outskirts of the jovian system would benefit from Galileo DDS data to be obtained during the *I33* and *A34* orbits (2002–2003), as well as from the Cassini CDA data obtained during its the Jupiter flyby (2000), which are as yet unavailable for analysis.

ACKNOWLEDGMENTS

We are grateful to Richard Holme for improving the style of the manuscript. Insightful and speedy reviews by Joseph A. Burns and an anonymous referee are appreciated. This work was funded by Deutsches Zentrum für Luft- und Raumfahrt (DLR), Projects 50 OH 0003 and 50 QJ 9503 3. I. W. acknowledges support by Universität Potsdam/Innovationskolleg.

REFERENCES

Burns, J. A., P. L. Lamy, and S. Soter 1979. Radiation forces on small particles in the Solar System. *Icarus* **40**, 1–48.

Burns, J. A., M. R. Showalter, J. N. Cuzzi, and J. B. Pollack 1980. Physical processes in Jupiter's ring—Clues to its origin by Jove! *Icarus* **44**, 339–360.

Burns, J. A., M. R. Showalter, and G. E. Morfill 1984. The ethereal rings of Jupiter and Saturn. In *Planetary Rings* (R. Greenberg and A. Brahic, Eds.), pp. 200–272. Univ. of Arizona Press, Tucson.

Burns, J. A., M. R. Showalter, D. P. Hamilton, P. D. Nicholson, I. de Pater, M. E. Ockert-Bell, and P. C. Thomas 1999. The formation of Jupiter's faint rings. *Science* **284**, 1146–1150.

Colwell, J. E., and L. W. Esposito 1990. A model of dust production in the Neptune ring system. *Geophys. Res. Lett.* **17**, 1741–1744.

Colwell, J. E., M. Horányi, and E. Grün 1998. Capture of interplanetary and interstellar dust by the jovian magnetosphere. *Science* **280**, 88–91.

Cruikshank, D. P., J. Degewij, and B. H. Zellner 1982. The outer satellites of Jupiter. In *Satellites of Jupiter* (D. Morrison, Ed.), pp. 129–146. Univ. of Arizona Press, Tucson.

Divine, N. 1993. Five populations of interplanetary meteoroids. *J. Geophys. Res.* **98**, 17,029–17,048.

Esposito, L. W., and J. E. Colwell 1989. Creation of the Uranus rings and dust bands. *Nature* **339**, 605–607.

Everhart, E. 1985. An efficient integrator that uses Gauss-Radau spacing. In *Dynamics of Comets: Their Origin and Evolution* (A. Carusi and G. B. Valsecchi, Eds.), pp. 185–202. Reidel, Dordrecht.

Grün, E., H. Fechtig, M. S. Hanner, J. Kissel, B.-A. Lindblad, D. Linkert, D. Maas, G. E. Morfill, and H. A. Zook 1992. The Galileo dust detector. *Space Sci. Rev.* **60**, 317–340.

Grün, E., B. Å. S. Gustafson, I. Mann, M. Baguhl, G. E. Morfill, P. Staubach, A. Taylor, and H. A. Zook 1994. Interstellar dust in the heliosphere. *Astron. Astrophys.* **286**, 915–924.

Grün, E., M. Baguhl, N. Divine, H. Fechtig, and 15 colleagues 1995a. Three years of Galileo dust data. *Planet. Space Sci.* **43**, 953–969.

Grün, E., M. Baguhl, H. Fechtig, D. P. Hamilton, J. Kissel, D. Linkert, G. Linkert, and R. Riemann 1995b. Reduction of Galileo and Ulysses dust data. *Planet. Space Sci.* **43**, 941–951.

Grün, E., H. Krüger, S. F. Dermott, H. Fechtig, and 17 colleagues 1997. Dust measurements in the jovian magnetosphere. *Geophys. Res. Lett.* **24**, 2171–2174.

Grün, E., H. Krüger, A. Graps, D. P. Hamilton, and 17 colleagues 1998. Galileo observes electromagnetically coupled dust in the jovian magnetosphere. *J. Geophys. Res.* **103**, 20,011–20,022.

Hamilton, D. P., and A. V. Krivov 1996. Circumplanetary dust dynamics: Effects of solar gravity, radiation pressure, planetary oblateness, and electromagnetism. *Icarus* **123**, 503–523.

Hamilton, D. P., and A. V. Krivov 1997. Dynamics of distant moons of asteroids. *Icarus* **128**, 241–249.

Horányi, M. 1994. New jovian ring? *Geophys. Res. Lett.* **21**, 1039–1042.

Horányi, M., J. A. Burns, M. Tátrallyay, and J. G. Luhmann 1990. Toward understanding the fate of dust lost from the martian satellites. *Geophys. Res. Lett.* **17**, 853–856.

Horányi, M., M. Tátrallyay, A. Juhász, and J. G. Luhmann 1991. The dynamics of submicron-sized dust particles lost from Phobos. *J. Geophys. Res.* **96**, 11,283–11,290.

Horányi, M., J. A. Burns, and D. P. Hamilton 1992. The dynamics of Saturn's E ring particles. *Icarus* **97**, 248–259.

Humes, D. H. 1976. The Jovian meteoroid environment. In *Jupiter: Studies of the Interior, Atmosphere, Magnetosphere and Satellites* (T. Gehrels, Ed.), pp. 1052–1067. Univ. of Arizona Press, Tucson.

Jacobson, R. A. 2000. The orbits of the outer jovian satellites. *Astron. J.* **120**, 2679–2686.

Kessler, D. J. 1981. Derivation of the collision probability between orbiting objects: The lifetimes of Jupiter's outer moons. *Icarus* **48**, 39–48.

Kimura, H., H. Ishimoto, and T. Mukai 1997. A study on solar dust ring formation based on fractal dust models. *Astron. Astrophys.* **326**, 263–270.

Krivov, A. V., and M. Banaszkiewicz 2001. Unusual origin, evolution and fate of icy ejecta from Hyperion. *Planet. Space Sci.* **49**, 1265–1279.

Krivov, A. V., H. Kimura, and I. Mann 1998. Dynamics of dust near the Sun. *Icarus* **134**, 311–327.

Krivov, A. V., H. Krüger, E. Grün, K.-U. Thiessenhusen, and D. P. Hamilton 2002. A tenuous dust ring of Jupiter formed by escaping ejecta from the Galilean satellites. *J. Geophys. Res.* **107**(E1), 10.1029/2000 JE 001434.

Krüger, H., E. Grün, D. P. Hamilton, M. Baguhl, and 18 colleagues 1999a. Three years of Galileo dust data: II. 1993 to 1995. *Planet. Space Sci.* **47**, 85–106.

Krüger, H., E. Grün, A. Heck, and S. Lammers 1999b. Analysis of the sensor characteristics of the Galileo dust detector with collimated jovian dust stream particles. *Planet. Space Sci.* **47**, 1015–1028.

Krüger, H., A. V. Krivov, D. P. Hamilton, and E. Grün 1999c. Detection of an impact-generated dust cloud around Ganymede. *Nature* **399**, 558–560.

Krüger, H., A. V. Krivov, and E. Grün 2000. A dust cloud of Ganymede maintained by hypervelocity impacts of interplanetary micrometeoroids. *Planet. Space Sci.* **48**, 1457–1471.

Krüger, H., and 20 colleagues 2001. One year of Galileo dust data from the jovian system: 1996. *Planet. Space Sci.* **49**, 1285–1301.

Landgraf, M., W. J. Baggaley, E. Grün, H. Krüger, and G. Linkert 2000. Aspects of the mass distribution of interstellar dust grains in the Solar System from in-situ measurements. *J. Geophys. Res.* **105**, 10,343–10,352.

Murray, C. D., and S. F. Dermott 1999. *Solar System Dynamics*. Cambridge Univ. Press, Cambridge.

Ockert-Bell, M. E., J. A. Burns, I. J. Daubar, P. C. Thomas, J. Veverka, M. A. S. Belton, and K. P. Klaasen 1999. The structure of Jupiter's ring system as revealed by the Galileo imaging experiment. *Icarus* **138**, 188–213.

Sheppard, S. S., D. C. Jewitt, Y. Fernandez, G. Magnier, B. G. Marsden, M. Holman, C. T. Kowal, E. Roemer, and G. V. Williams 2000. S/1975 J 1 = S/2000 J 1. IAU Circ. No. 7525.

Sheppard, S. S., D. C. Jewitt, Y. Fernandez, and G. Magnier 2001. *Satellites of Jupiter*. IAU Circ. No. 7555.

Sykes, M. V., B. Nelson, R. M. Cutri, D. J. Kirkpatrick, R. Hurt, and M. F. Skrutskie 2000. Near-infrared observations of the outer jovian satellites. *Icarus* **143**, 371–375.

Thiessenhusen, K.-U., H. Krüger, F. Spahn, and E. Grün 2000. Large dust grains around Jupiter—The observations of the Galileo dust detector. *Icarus* **144**, 89–98.

Throop, H. B., and L. W. Esposito 1998. G ring particle sizes derived from ring plane crossing observations. *Icarus* **131**, 152–166.

Zook, H. A., and S.-Y. Su 1982. Dust particles in the jovian system. *Lunar Planet. Sci.* **XIII**, 893–894.